The Au-ZrO_2 Interface: Energy and Morphology

Ting Mao

The Au-ZrO_2 Interface: Energy and Morphology

Research Thesis

In Partial Fulfillment of the

Requirements for the Degree of

Master of Science in Materials Engineering

Ting Mao

Submitted to the Senate of the Technion-Israel Institute of Technology

Elul 5778 Haifa August 2018

This research thesis was conducted under the supervision of **Prof. W.D. Kaplan** in the Department of Materials Science & Engineering at the Technion.

Acknowledgements

I would like to thank my supervisor Prof. Wayne D. Kaplan for his patience, inspiration and encouragement during the past two years. For encouraging me to learn everything, teaching me the importance of conducting independent research, and guiding me from the very beginning to learn how to do research. I also would like to thank him for the help and inspiring conversation to help me get through difficulties in living in a foreign country.

I wish to thank all the friends and colleagues from the Metal-Ceramic Interface Lab for their help and support: Rachel Marder Jaeckel, Hadas Sternlicht, Hadar Bratt-Nahor, Ruth Moshe, Leon Rudnik, Ismail Nassar and Liora Mizrahi Tsyganok. Special thanks to Rachel and Hadas for all the help with my study and life in Israel, starting from me getting off the train from Ben Gurion airport in to Haifa in 2016.

I would like to thank the MIKA staff: Michael Kalina, Dr. Alex Berner, Dr. Yaron Kauffmann, Dr. Galit Atiya, Dr. Anna Kosinova and Dr. Maria Koifman. For all the help with the sample preparation and characterization. It has been a great privilege to learn from all of them.

I want to thank the ISF for the financial support throughout this study.

I want to thank all the friends I met because of these two years in Israel and the one-month back at Shantou in 2014, when I joined the summer course held by Technion and Shantou University. These are very special times in my life. Finally, I would like to thank my family for their support and encouragement all the time.

Table of Contents

The Au-ZrO_2 Interface: 1

The Au-ZrO_2 Interface: I

Acknowledgements II

Table of Contents I

List of Figures I

List of Tables VI

Abstract 1

List of Symbols and Abbreviations 2

1. Literature Survey 4

1.1 Surface Energy of Solids 4

1.1.1 Surface Energy Anisotropy (Theoretical and Experimental) 4

1.1.2 Equilibrium Crystal Shape of Solid (Wulff Construction) 5

1.1.3 Surface Anisotropy Dependence on Temperature and Segregation 6

1.2 Metal-Ceramic Interfaces 7

1.2.1 Solid-Liquid Interface 7

1.2.2 Wetting versus Dewetting 9

1.2.3 Solid-Solid Interface 10

1.2.4 Interface Chemistry and Thermodynamics 14

1.3 Dewetting of Thin Films 16

1.3.1 Solid and Liquid State Dewetting 16

1.3.2 Shape Evolution of Solid Particles 17

1.4 Au-YSZ Interface 18

1.4.1 Gold 19

1.4.2 YSZ 20

2. Research Goals 22

3. Experimental Methods 23
3.1 Dewetting Experiments 23
3.1.1 Solid-State Dewetting in a Controlled Atmosphere 23
3.1.2 Liquid and Solid State Dewetting in Air 24
3.2 TEM Sample Preparation 24
3.3 SEM and TEM Characterization 25
3.3.1 Characterization and Simulation of Au Morphology 25
3.3.2 Orientation Relationship Characterization 26
3.3.3 Interface Chemistry Characterization 28
4. Results 30
4.1 Solid-State Dewetting in a Controlled Atmosphere 30
4.1.1 Initial Solid-State Dewetting Experiments 30
4.1.2 Second Set of Solid-State Dewetting Experiments 43
4.2 Solid and Liquid State Dewetting in Air 49
4.2.1 Dewetted Au Particle Morphology 49
4.2.2 Preferred Orientation 52
5. Discussion 54
5.1 Solid-State Dewetted Particle Morphology 54
5.1.1 Non-Equilibrated Morphology 54
5.1.2 Equilibrated Morphology 55
5.2 Interface Energy and Interface Structure 56
5.3 Interface Chemistry and Interface Structure 58
5.4 The Difference between Solid and Liquid State Dewetting 59
5.4.1 Interface Preferred Orientation 59
5.4.2 Grain Boundaries and Liquid State Dewetting 61
6. Summary and Conclusions 62
7. Suggestions for Future Work 63

8. References..... 64

אנרגיה ומורפולוגיה של משטחי ביניים בין ZrO_2-ל Au I

אנרגיה ומורפולוגיה של משטחי ביניים בין ZrO_2-ל Au II

List of Figures

Figure 1: Two-dimensional illustration of a Wulff construction drawn with Mathematica. (a) An example of surface energy anisotropy where the γ-plot (in red) is a function of orientation θ. (b) Perpendicular lines at the end of each γ(θ) vector form a closed hexagonal shape (blue) defining the ECS. (c) The ECS defined by the cusps from the (red) γ-plot..... 6

Figure 2: Schematic drawing of the geometry of a liquid drop in contact with a solid substrate. (a) The solid-liquid interface is co-planar with the substrate surface and equilibrated at a contact angle of θ. (b) The solid-liquid interface is curved. The dihedral angles are indicated (θ_V, θ_L, θ_S). (c) Ridging at the triple junction of a substrate in contact with a liquid drop. 9

Figure 3: Variables describe a grain boundary plane x_A; y_A;z_A and x_B , y_B , z_B are the axes of the coordinates parallel to crystallographic directions in grains A and B, respectively. o is the rotation axis and is the rotation (misorientation) angle necessary to transfer both grains to an identical position. n determines the orientation of the grain boundary plane. The illustration was reproduced from [22]. 10

Figure 4: Schematic drawing of a solid single crystal in contact with a flat solid surface. In (b) segregation to the interface has resulted in a large area of contact than in (a), due to a lower interface energy. This is not reflected in the contact angle, which is identical for both cases because of faceting of the particle.12

Figure 5: Schematic drawing of the Winterbottom analysis for particles equilibrated on a substrate having an effective contact angle larger than 90°. The blue polyhedron is an equilibrated single crystal in contact with a solid substrate, and the red curve is the Wulff shape. 13

Figure 6: Schematic density variation across a solid-vapor interface[37]. 14

Figure 7: Schematic drawing of solid-state dewetting of polycrystalline thin film on a substrate. (a)–(d) show grain boundary grooving starting from the free surface until it hits the substrate; (e)–(h) show voids nucleation and growth towards the free surface. Illustration from [48]. 17

Figure 8: Equilibrium crystal shapes of gold from literature. (a) Equilibrated Au particle on graphite under UHV(1000˚C) [62,65]; (b) Equilibrated Au on α-SiC under UHV(900˚C) [63]; (c) Equilibrated Au on (1000) sapphire in air(1000˚C) [68]; (d) Left bottom: Wulff shape of equilibrated Au on (110) TiO_2 in air(500-700˚C). The graph at the right corner is a STEM micrograph of an equilibrated Au nano-crystal on TiO_2 with a Wulff shape fitted to the Au particle [64].....20

Figure 9: Phase diagram for the ZrO_2-rich part of the ZrO_2-Y_2O_3 system. The marked region indicates non-equilibrium monoclinic-tetragonal transition (redrawn after [71]).....21

Figure 10: Schematic drawing of the sapphire tube furnace used for the dewetting experiments.....24

Figure 11: Illustration of FIB in-situ lift-out process: (a) A selected equilibrated gold particle is marked and protected with carbon deposition; (b) A "U-cut" is made by gallium ion milling at both side of the selected the particle; (c) A needle is attached to the lamella; (d) Lift-out of the lamella; and (e) The lamella is attached to a TEM grid followed by (f) thinning of the lamella. 25

Figure 12: Illustration for basic set-up of a diffractometer. X-ray tube is the x-ray source. 27

Figure 13: Areas of EDS acquisition for spatial difference.....29

Figure 14: Sample surface morphology after dewetting at 950˚C under flowing Ar + 7vol.% H_2 for 48 hours. 30

Figure 15: Secondary electron HRSEM micrograph of an equilibrated Au particle after solid state dewetting, which was equilibrated at 950˚C under flowing Ar + 7vol.% H_2 for 48 hours. 31

Figure 16: SEM micrographs showing representative morphologies of non-equilibrated particles. (a) An elongated non-equilibrated Au particle; (b) Equi-axed Au particle with unbalanced facet area for the {111} family of planes. 32

Figure 17: Secondary electron micrograph showing a sharp edge around the facets....32

Figure 18: (a) Wulffmaker simulation of the gold equilibrium crystal shape according to the experiment results. (b) HRSEM graph of an equilibrated gold particle from solid state dewetting. 33

Figure 19: XRD patterns from a sample after dewetting, where (b) is a magnified angular range compared to (a). 34

Figure 20: XRD from an as-deposited sample, where (b) and (c) are two magnified angular ranges compared to (a). 35

Figure 21: EBSD orientation relationship results of equilibrated Au particles on (111) YSZ. (a) EBSD pole figures in 3 different pole directions for 150 equilibrated gold particles from the first solid-state dewetting; (b) orientation of (111) YSZ substrate. 36

Figure 22: (a) (b) (c) Bright field TEM image of three equilibrated gold particles (black area) along with parts of the YSZ substrate. (d) (e) (f) Selected area diffraction patterns taken from the Au-YSZ interface region. Reflections from Au particles are marked in yellow, and reflections from YSZ are marked in blue. Both the BF micrographs and diffraction patterns were acquired after aligning the particle to **[$\bar{1}$10]** zone axis. 37

Figure 23: Winterbottom analysis of an equilibrated Au particle. The yellow outline is the Wulff shape of the Au crystal. The distance from the Wulff center to the interface and uppermost (111) facet of Au are marked as R_1 and R_2, respectively. 38

Figure 24: (a) HAADF STEM micrographs of the interface of particle (c) in Figure 22. (b) HAADF STEM micrograph combined with EDS elemental mapping showing Ca segregation colored in purple at the interface. 39

Figure 25: (a) The region from which an EDS line-scan across the interface was acquired. (b) EDS line-scan data showing an excess of Ca at the interface. 40

Figure 26: Spatial difference analysis of a Au-YSZ interface. (a) Uppermost spectrum in red is the EDS spectra from half of the EDS scanning box in the Au particle. The spectrum in the middle in black is the EDS spectra acquired from the interface region (the red square in the spectra marks the Ca peak). The spectra at the bottom is from half of the scan-box in the YSZ substrate.

(b) Magnified Ca peak from the Au, interface, and YSZ, showing the clear existence of Ca exess at the interface. 41

Figure 27: Spatial difference spectrum from the (111) Au free surface. (a) presents the three EDS spectrum from Au bulk, (111) Au surface area, and the carbon layer next to the (111) Au surface. (b) is the magnified segment from (a) showing no Ca excess on the (111) surface. 42

Figure 28: XRD pattern from a sample after solid-state dewetting: (a) is the full pattern acquired from 20° to 80°; (b) is a segment of (a) and only includes reflections from the gold particles. 43

Figure 29: XRD pattern from the as-deposited sample after improved substrate cleaning. (a) Full spectrum includes signals from polycrystalline Au thin film and the single crystal (111) YSZ substrate, ranging from 20° to 80°. (b) (c) Segments of (a) that include all reflections of Au. 44

Figure 30: EBSD orientation relationship result of equilibrated Au particles (second dewetting experiment) and YSZ. (a) EBSD pole figures in 3 different pole directions of 150 equilibrated gold particles from the second solid state dewetting; (b) orientation of (111) YSZ substrate. 45

Figure 31: Bright field TEM micrographs of three equilibrated gold particles (black contrast) equilibrated on the YSZ substrate. (d), (e), and (f) are selected area diffraction patterns acquired from the interface region from (a), (b), and (c), respectively. All three particles were aligned in the **[$\bar{1}$10]** zone axis before acquiring the micrographs and diffraction patterns. 46

Figure 32: (a) HAADF STEM image of the interface of particle (a) in Figure 31. HAADF STEM image combined with EDS elemental mapping showing Cr segregation colored in blue at the interface, as well as Y segregation to the YSZ surface marked in red. 47

Figure 33:: (a) Arrow of line scan across the interface in STEM EDS elemental mapping. (b) Line scan spectrum showing Cr and Y quantification at each position of the line scan arrow across the interface. 48

Figure 34: (a) EDS spatial difference result from the particle in Figure 31(c). The spectrum in red is the EDS signal from the bulk Au particle (away from the

interface). The spectrum in black is the EDS signal from the interface region. The spectrum in blue is the EDS signal from the bulk YSZ (away from the interface). (b) Enlarged peak of Cr from the Au, interface and YSZ regions, showing Cr excess at the interface. 49

Figure 35: SEM plan-view micrograph of a sample after solid-state dewetting in air. 50

Figure 36: SEM micrographs of (a) Au particles on the YSZ surface after liquid-state dewetting in air. (b) is a higher magnification micrograph of single crystalline and polycrystalline Au particles. The particles were equilibrated at 1000˚C for 48 hours after the liquid-state dewetting. 50

Figure 37: HRSEM micrographs showing the Au particle morphology with different preferred orientations, after liquid-state dewetting in air, followed by annealing at 1000˚C for 48 hours. (a) Particle showing an orientation of Au {100} ‖ YSZ{111}; (b) Particle showing an orientation of Au{111} ‖ YSZ{111}; (c) Particle showing an orientation of Au {110}‖YSZ{111} 51

Figure 38: Morphology of Au particles with grain boundaries and steps. Particles were annealed at 1000˚C for 48 hours after liquid-state dewetting in air. (a) Bi-crystalline Au particle showing a twin; (b) Polycrystalline Au particle showing multiple twins; (c) A particle showing steps on {100} facet planes that outline the facet shape. 51

Figure 39: An XRD pattern from a sample after liquid-state dewetting. (a) is the full pattern acquired from 20° to 117°. (b) and (c) are segments of (a) and only include reflections from the gold particles. 52

Figure 40: (a) Au particle found to be slightly curved (as indicated by the arrow); (b) Elongated Au particle. 55

Figure 41: Illustration from [81]. (a)-(b) Initial stage of bi-crystal shape evolution towards elongated single crystal. 55

Figure 42: EBSD results showing orientation of equilibrated Ni and Au particles on (111) YSZ substrates. (a) for Ni from [35]; (b) from Au/(111)YSZ with Ca segregation; (c) from Au/(111)YSZ with Cr segregation. 57

List of Tables

Table 1: Surface energy anisotropy between (100) and (111) of Au from literature. ... 19

Table 2: Standard random intensity of Au [77]. ... 28

Table 3: Comparison of relative surface energies $\gamma_{\{hkl\}}/\gamma_{\{111\}}$ between simulation and experiment. ... 33

Table 4: P ratio results from dewetted and as-deposited gold. ... 35

Table 5: Interface energy results from particle (a), (b) and (c). See Figure 22. ... 38

Table 6: P ratio results of the second solid state dewetting experiments. ... 44

Table 7: Interface energy results from particle (a), (b), and (c) in Figure 31. ... 47

Table 8: P ratio of the particles after liquid and solid-state dewetting. ... 53

Abstract

Metal-ceramic interfaces have numerous applications in composite materials, thermal barrier coatings, solid oxide fuel cells, etc. As such, a fundamental understanding of metal-ceramic interface energetics and structure is important since they define the overall function of the system. In this work, thin films of gold were deposited on (111) oriented yttria stabilized zirconia (YSZ) substrates and annealed at high temperatures until the films "dewetted" and equilibrated.

Two sets of solid-state dewetting experiments in reducing atmosphere were conducted. Equilibrated interfaces from the two experiments were found to have Ca or Cr adsorption by scanning transmission electron microscopy (STEM) combined with energy dispersive spectroscopy (EDS). Interfaces with an excess of Cr were found to have a lower energy than interfaces with an excess of Ca. 150 equilibrated particles from both experiments were characterized by electron backscattered diffraction (EBSD) and were found to have a random in-plane orientation relationship, but with a strong out of plane preferred orientation, which is {111} Au || {111} YSZ. This was corroborated by X-ray θ-2θ characterization. It was also found that the strong preferred orientation exists before dewetting.

Liquid and solid-state dewetting experiments were also conducted in air, where liquid dewetting resulted in a more isotropic orientation of {111} Au|| {111} YSZ than for solid-state dewetting.

Although no pure Au-(111) YSZ interface was characterized, based on comparisons with other systems it can be assumed that Ca/Cr segregation reduces the anisotropy, resulting in a preferred orientation instead of a low-index orientation relationship (e.g. for Ni on (111) YSZ). Liquid-state dewetting changed the pre-existing preferred orientation of {111} Au || {111} YSZ of the as-deposited film, resulting in a more isotropic preferred orientation compared to solid-state dewetting. This may be due to the heterogeneous nucleation process occurring during the course of liquid-state dewetting.

List of Symbols and Abbreviations

BF	Bright field
c	Atomic concentration
DFT	Density functional theory
D_s	Surface diffusion coefficient
EBSD	Electron backscatter diffraction
ECS	Equilibrium crystal shape
EDS	Energy dispersive spectroscopy
FEG	Field emission gun
FCC	Face centered cubic
FIB	Focused ion beam
HAADF	High angle annular dark field
HRTEM	High resolution transmission electron microscopy
I_A, I_B	Measured x-ray intensity of element A and B, respectively
ICDD	International Center for Diffraction Data
k	Boltzmann's constant
n	Number of moles
n	Grain boundary plane normal
R_1, R_2	Distance between the Wulff point and the surface of the substrate and between the Wulff point and one of the facets of the particle, respectively
SAD	Selected area diffraction

SEM	Scanning electron microscopy
STEM	Scanning transmission electron microscopy
T_m	Melting temperature
T_R	Roughening temperature
TEM	Transmission electron microscopy
UHV	Ultra-high vacuum
XRD	X-ray diffraction
YSZ	Yttria stabilized zirconia
σ	Interface
γ	Surface or interface energy
μ	Chemical potential
γ_{LV}	Liquid-vapor interface energy (liquid surface energy)
γ_{PV}	Particle-vapor interface energy (particle surface energy)
γ_{SL}	Solid-liquid interface energy
γ_{SP}	Substrate-particle interface energy
γ_{SV}	Substrate-vapor interface energy (substrate surface energy)
ν_{at}	Number of atoms per unit surface area
τ_{eq}	Equilibration time
Ω	Atomic volume
Γ	Interfacial excess

1. Literature Survey

1.1 Surface Energy of Solids

1.1.1 Surface Energy Anisotropy (Theoretical and Experimental)

Surface energy can be defined as the excess energy of a surface of a material compared to its bulk. This excess energy originates from the fact that many of the neighboring atoms are missing for atoms at the surface compared to in the bulk. Consider a simple FCC crystal as an example, where each atom inside the bulk is supposed to have 12 nearest neighbor atoms. Atoms at the (100), (110) and (111) surface have respectively 4, 5, 3 unsaturated bonds, these broken bonds are what makes each surface has an exceeding and distinguished energy compare to the bulk.

Theoretically one can say that the surface energy can be determined as the total energy of the unsaturated nearest neighbor bonds divided by surface area of the reference atom. While the broken bond model sounds straightforward and applicable, it does have its limitation in predicting surface energies. For solids, atoms are arranged in a different way for different orientations, thus surface energies for solids are anisotropic. While the broken bond model can be applied to predicting the surface energy for ideal surfaces, surface relaxation, reconstruction, and surface charge smoothing are ignored in this approach [1]. Galanakis et al. compared the broken bond model to density functional theory (DFT) simulations, and found a good agreement for the prediction of surface energy anisotropy of FCC noble metals, but a larger deviation was found in transition metals and sp metals [2]. While the broken-bond estimation is crude, it can serve as a non-relaxed estimation for comparison with other theoretical approaches, which include fundamental first principle electronic structure calculations in the framework of DFT [3] and less fundamental semi-empirical approaches when a large number of atoms are needed [4].

Surface energy predictions by theoretical calculations appears straightforward, and the absolute surface energy can be obtained, but different approximations (models) can deviate significantly from each other [2]. Measurement of surface energies for real materials is difficult and limited data for surface energy anisotropy of solids exists [5]. Most of the surface energy data recorded in the past were measured at high temperatures

from liquid surfaces, and extrapolated to lower temperatures ignoring surface anisotropy[6,7].

1.1.2 Equilibrium Crystal Shape of Solid (Wulff Construction)

For isotropic materials in a homogeneous environment without gravity, energy minimizing results in a spherical shape. Surface energies of solids are known to be anisotropic. Thus energy minimization by shape changes of a solid does not result in a sphere (which has the smallest surface area but not necessarily the lowest energy), nor a polyhedron constructed by facets with only the lowest surface energies. Usually the minimized surface energy results in a crystal shape between the two extremes. The Wulff construction is a thermodynamic graphical construction that can predict the energy minimizing equilibrium crystal shape for a known surface energy anisotropy [8]. The Wulff construction was developed based on experimental observations [9] of natural crystals by Wulff, and was mathematically explained by von Laue [10] and Dinghas [11].

Wulff's theorem basically says that for an equilibrium crystal shape, the ratio between distances from the Wulff center to each facet plane and the surface energy of each facet plane should be constant for a given crystal:

$$\frac{\gamma_1}{R_1} = \frac{\gamma_2}{R_2} = \ldots = \frac{\gamma_i}{R_i} = \text{constant} \qquad \rightarrow \qquad \frac{\gamma_i}{\gamma_j} = \frac{R_i}{R_j} \tag{1}$$

Figure 1 presents a schematic drawing of a two-dimensional example of a Wulff construction. If we draw at the end of each surface energy vector a perpendicular line in the γ plot, there will be a closed envelope inside all the lines which defines the equilibrium crystal shape of the given γ plot. Since the equilibrium crystal shape is an energy minimized shape, one may find that the inner envelope is a polyhedral shape (for the three dimensional case) with truncated facets defined from deep cusps in the gamma plot.

While the Wulff construction is about extrapolating geographical form of equilibrium crystal shape from a known γ plot. In a reverse sense, if morphology details of an equilibrium crystal form is known, i.e. the distances from the Wulff center to each of the equilibrated facet plane, we will be able to extract the relative surface energy according

to Equation (1). If one of the absolute surface energies of the facets is known, we can obtain the absolute energies of other facet planes. The inverse Wulff construction was conducted before by Chatain et al. in extracting γ plot of Cu from morphology of equilibrated Cu particles from dewetting experiment [12].

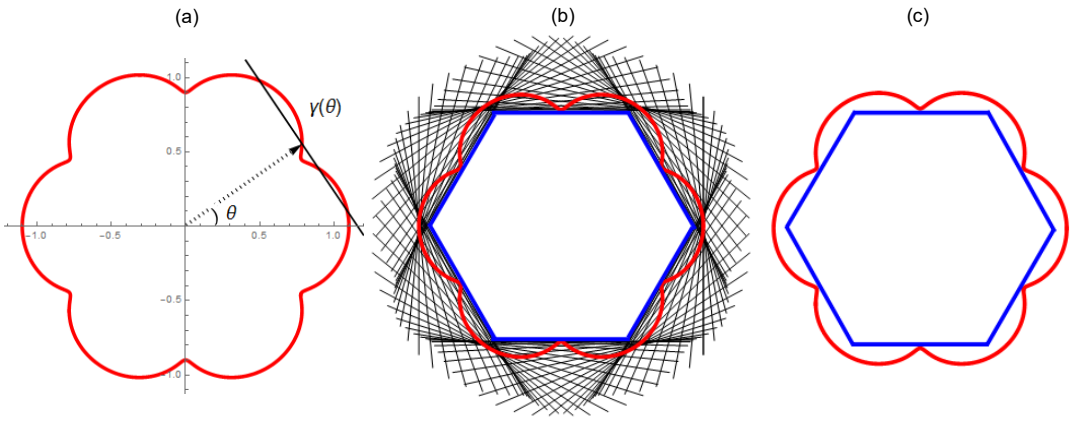

Figure 1: Two-dimensional illustration of a Wulff construction drawn with Mathematica. (a) An example of surface energy anisotropy where the γ-plot (in red) is a function of orientation θ. (b) Perpendicular lines at the end of each γ(θ) vector form a closed hexagonal shape (blue) defining the ECS. (c) The ECS defined by the cusps from the (red) γ-plot.

1.1.3 Surface Anisotropy Dependence on Temperature and Segregation

Temperature is known to have significant influence on surface anisotropy [13]. Extreme case to show temperature effect on surface anisotropy would be faceted equilibrium crystal shape at 0 K corresponding to a γ-plot with deep cusps at the facet direction. If the temperature is raised to above the melting point, the shape of the crystal will be a sphere (in an isolated case) which corresponds to a rounded γ-plot in any direction. However, anisotropy change due to temperature actually happens even before reaching the melting point and this is termed as roughening of surfaces. Roughening of metal surfaces was elaborated extensively by Lapujoulade [14]. Flat facet on ECS without any defect or steps is known to be kinetically stable and of low energy and it is connected to

the deep cusps on the γ-plot. Steps on the vicinal surface of facet are the reason for its extra energy compared to the lowest energy at the cusp which is the energy of the flat facet. When the temperature increases, motion of the steps can be wavy and extend to the flat area replacing the flat surface when the temperature increases to some certain value termed as the roughening temperature T_R. As a result, a flat facet will be roughened and cusps in γ-plot will disappear. This phenomenon is called the "roughening transition" [14].

Surface energy anisotropy of solids can also be affected by a change in chemical composition of the surface, via adsorption or segregation. From a thermodynamic point of view there is no difference between the two. However, it is accepted convention to define segregation as the reduction of surface energy because of a component arriving to the surface from the bulk [15]. Adsorption is usually used to describe the same process, but when the species arrive from the gas phase [16,17]. An introduction on how segregation/adsorption will change surface energies will be shown in 1.2.4.

1.2 Metal-Ceramic Interfaces

1.2.1 Solid-Liquid Interface

Equilibrated states of a liquid on a solid surface can be described by the contact angle θ at the liquid-vapor-solid triple junction, which within the limits of an interface which is flat and co-planar with the surface can be interpreted by Young's equation:

$$\gamma_{SV} = \gamma_{SL} + \gamma_{LV} \cos\theta \qquad (2)$$

where γ_{SV}, γ_{SL} and γ_{LV} are the solid-vapor, liquid-vapor and liquid-solid interface energies, respectively.

Since the contact angle is a measurable parameter, if two of the surface energies are known, we can extract the third surface energy. Equation (2) can be written as:

$$\gamma_{LV} \cos\theta = \gamma_{SV} - \gamma_{SL} \qquad (3)$$

The right side of Equation (3) resembles part of the expression of an important thermodynamic parameter, which is the thermodynamic work of adhesion (see Equation (4)). The work of adhesion can be described as the energy expended/gained for two different free surfaces to form an equilibrated interface. It is an important parameter that characterizes the bonding property of two materials.

$$W_{ad} = \gamma_{LV} + \gamma_{SV} - \gamma_{LS} \tag{4}$$

Combining equation (3) and (4) yields the Young-Dupre equation:

$$W_{ad} = \gamma_{LV}(1 + \cos\theta) \tag{5}$$

If the surface tension of the liquid is known (or measured from the shape of a sessile drop [18]), we can determine the work of adhesion.

Young's equation is only valid when the solid-liquid interface is flat and co-planar with the surface of the substrate (see Figure 2(a)). Thus, this equation is limited to cases where the solid is rigid and insoluble when it is in contact with a liquid. For substrates that are deformable in contact with liquids, then Figure 2(b) applies. The equilibrated state at the triple junction is composed of a balance of both parallel and vertical forces, with respect to the substrate surface. The vertical force balance here is reached at the expense of a deformed interface, thus Young's equation is no longer applicable to describe the equilibrated state at the triple junction. The equilibrated triple junction is usually described using the sine rule [19]:

$$\frac{\gamma_{SL}}{\sin\theta_V} = \frac{\gamma_{SV}}{\sin\theta_L} = \frac{\gamma_{LV}}{\sin\theta_S} \tag{6}$$

where θ_V, θ_L and θ_S are the dihedral angles in the vapor, liquid and substrate phase respectively.

For the case of wetting experiments conducted at high temperature, ceramic surfaces such as alumina which are usually rigid and stable, are found to form ridges at the triple junction when in contact with molten metal drops [19,20] (see Figure 2(c)).

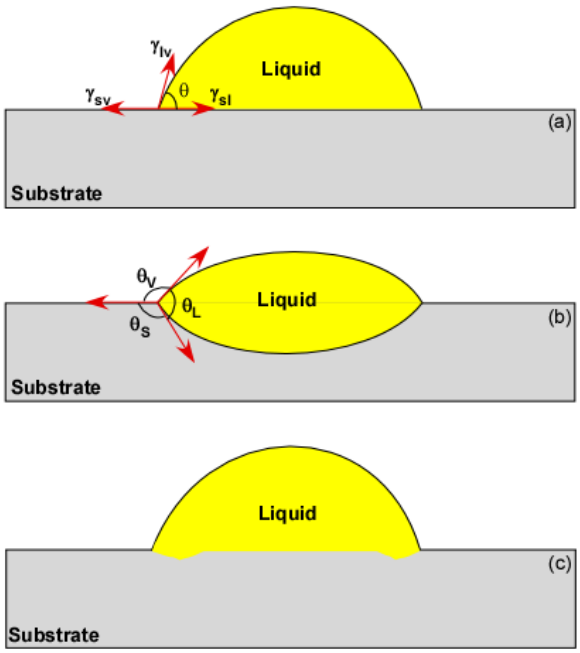

Figure 2: Schematic drawing of the geometry of a liquid drop in contact with a solid substrate. (a) The solid-liquid interface is co-planar with the substrate surface and equilibrated at a contact angle of θ. (b) The solid-liquid interface is curved. The dihedral angles are indicated (θ_V, θ_L, θ_S). (c) Ridging at the triple junction of a substrate in contact with a liquid drop.

1.2.2 Wetting versus Dewetting

Wetting experiments to extract interface energies by measuring the equilibrated contact angle at the three phase line are also called sessile drop experiments. One of the advantages of the sessile drop experiment is that the contact angle can be monitored in-situ [19,21].

Another way to obtain liquid droplets on solid substrate is the dewetting experiment. For metal and ceramic system, such experiments are conducted at high temperatures in order to bring the metal to a liquid state. After dewetting, a large number of sub-micron droplets can be obtained, thus ensuring good statistics. The drawback of this method may be the significant time to break the film to agglomerate and equilibrate on the substrate. The other is that is not easy to monitor the process in-situ, and the morphology of the droplets might change during the cooling process for ex-situ analysis[17]. Since

the droplets solidify during the cooling process, the shape of the liquid can't be determined.

1.2.3 Solid-Solid Interface

1.2.3.1 Interface Structure

Five macroscopic degrees of freedom are needed to describe a grain boundary, where two dissimilar grains meet. One way to describe the five degrees of freedom is illustrated in Figure 3. Two degrees of freedom are required for the grain boundary plane normal **n**. Three others for the relative orientation of the two grains; one is the rotation θ, the other two are the tilt angles for rotation axis **o**.

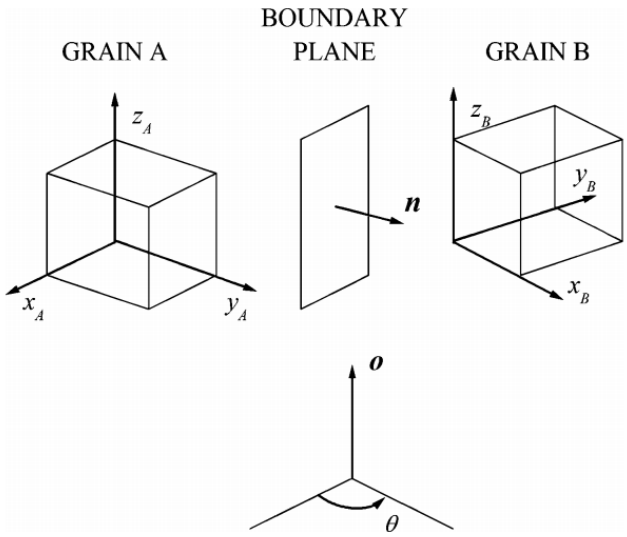

Figure 3: Variables describe a grain boundary plane x_A; y_A;z_A and x_B , y_B , z_B are the axes of the coordinates parallel to crystallographic directions in grains A and B, respectively. o is the rotation axis and is the rotation (misorientation) angle necessary to transfer both grains to an identical position. n determines the orientation of the grain boundary plane. The illustration was reproduced from [22]**.**

The three degrees of freedom to describe the orientation relationship of two grains are also referred to as Euler angles when orientation of a crystal need to be described in respect to a reference coordinate. Similar to grain boundaries, interface crystallography may also be described by five macroscopic degree of freedom.

In certain cases, special preferred orientation and orientation relationships are dominant among all the other configurations due to the tendency to minimize the interface/surface energy by reaching the maximum saturated bonds at the interface/surface. From a

macroscopic point of view, Fecht and Gleiter proposed a 'lock-in' model for metal and ionic crystals in contact with each other, where the interface is preferred to be arranged in such a way that the interface energy will be minimized [23]. The model suggests that in order for a low energy interface to form, the metal crystal will arrange its close-packed rows of atoms lying into the valleys of the close packed rows (lock-in) of the ionic crystal so that interatomic bonds of the two dissimilar lattices will be as saturated as possible. Also, the model took Cu/MgO and Au/KCl (14% and 35% misfit) as evidence to show that for systems with larger lattice mismatch, the more likely that there exists dominant orientation relationship with low interface energy, i.e. cube/cube, since these are the last ones with considerable number of lock-in mechanisms. The model also predicts correctly orientation relationships of Au/sapphire and Cu/sapphire[24] systems according to experimental results. However, as the authors themselves pointed out, the chemical nature of different systems is not taken into account in this model.

Although this model only correlates geometrical matching to low energy interface configurations, it can provide some insights for unrelaxed interfaces. However, more careful investigation is needed to understand these preferred configurations; going beyond the simple five degrees of freedom and taking into account the local atomistic structure and chemistry. The structure near the interface is more complicated than two unrelaxed lattices joined together, since strain exists due to lattice mismatch, and relaxation and/or reconstruction can happen which will change the distribution of atoms at the interface [25]. Moreover, the interatomic bonding strength might also affect the overall atomistic structure as well as the macroscopic orientation relationship. Since the 1990s, atomistic studies taking into account relaxation, reconstruction and interface chemistry have be carried out both experimentally (HRTEM atomistic imaging) [26–28] and theoretically (first principle calculations) [28–31].

1.2.3.2 Solid-Solid Interface Energy Measurement (Winterbottom Analysis)

Liquid-solid interface energy measurements can straightforward if the interface is flat and co-planar with the surface of the substrate (ideal sessile drop configuration). However, for solid-solid interfaces, due to the anisotropic nature of solid surfaces, the contact of two solids is more complicated and contact angles or dihedral angles cannot provide for accurate interpretation of the interface energy. Many experiments were done at high temperatures for liquids in contact with solids, and then attempts were made to

extrapolate interface energies to lower (solid state) temperatures, however these results cannot provide information with orientation dependence for solids [2,5,6]. According to Howe, the difference of surface energy at temperatures above and below the melting point can be about 20% [25]. This is one uncertainty from the surface energy of the solid affecting the accuracy of contact angle method.

Another reason for not using contact angle measurements for solids is that a reduction in the energy of the interface can happen due to interfacial segregation. As a result, the contact area will grow larger without a change in the contact angle at the triple line. If we measure the energy using the contact angle for the two different cases in Figure 4, the interface energies will be the same, however we know that the interface energy for (b) is lower than (a). Surface energy as well as its' temperature dependence, and contact angle independence from interface energy for solid-solid systems can introduce significant errors.

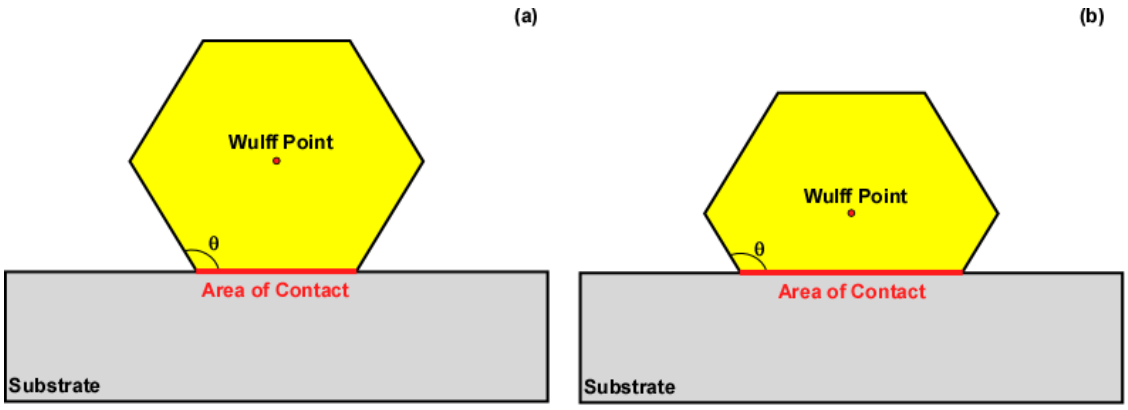

Figure 4: Schematic drawing of a solid single crystal in contact with a flat solid surface. In (b) segregation to the interface has resulted in a large area of contact than in (a), due to a lower interface energy. This is not reflected in the contact angle, which is identical for both cases because of faceting of the particle.

For solid-solid interfaces, a different approach is required. One successful method is Winterbottom's approach which analyzes the equilibrium crystal shape of a single solid crystal equilibrated on a foreign isotropic solid substrate [32]. A schematic introduction to the Winterbottom analysis is presented in Figure 5, resulting in:

$$\frac{R_1}{R_2} = \frac{\gamma_{SP} - \gamma_{SV}}{\gamma_{PV}} \tag{7}$$

where γ_{SP} is the substrate-particle interface energy, γ_{SV} is the surface energy of the substrate and γ_{PV} is the energy of one of the facets of the particle. R_1 is the distance measured from the Wulff center of the particle to the interface. R_2 is the distance measured from the Wulff center to the facet corresponding to the surface energy γ_{SV} [32,33].

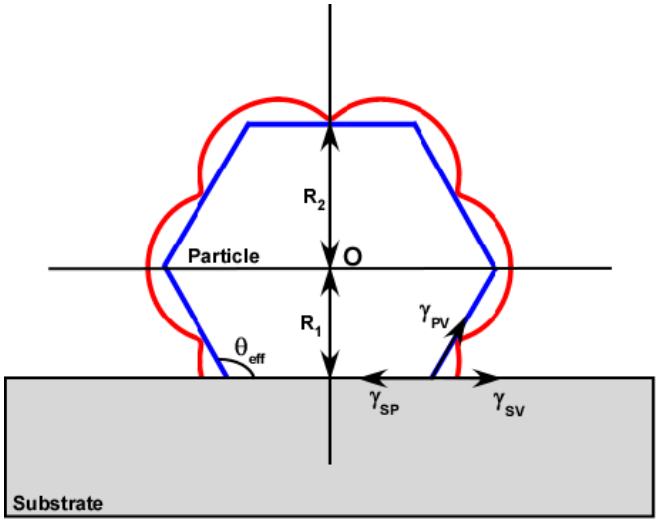

Figure 5: Schematic drawing of the Winterbottom analysis for particles equilibrated on a substrate having an effective contact angle larger than 90°. The blue polyhedron is an equilibrated single crystal in contact with a solid substrate, and the red curve is the Wulff shape.

To perform accurate interface energy analysis using the Winterbottom methodology, accurate absolute surface energies are required, however energy values of surfaces taking into account for surface anisotropy are hard to obtain and scarce in the literature or any databases [5]. Another source that can affect the accuracy is from the measurement of distance from the Wulff center to facets or interface. Particle used for this analysis needs to be fully equilibrated to get the distance under equilibrium condition [34]. Also in some special cases like dewetting of Ni on YSZ [35], ridging of the substrate surface at the triple line can happen, which means the interface plane and substrate surface is no longer co-planar. This discrepancy of R_1 should be taken into account as error in the final result.

1.2.4 Interface Chemistry and Thermodynamics

Gibbs Adsorption Isotherm

Interfacial segregation is known to have a significant effect on many properties of materials. Take polycrystalline materials as an example; grain boundary segregation can be the reason for change in grain boundary energy distribution, crystallographic texture, growth of grains, etc. These change will influence mechanical and general functional properties of the entire system [36]. Since interfaces exist in any system that requires contact of different materials, interfacial segregation is importance to study.

Gibbs proposed a thermodynamic model to describe the change of interface/surface energy in relation to interfacial segregation. An interface from a microscopic of view is not sharp, where a solid-vapor interface is taken as an example in Figure 6. Distribution of the solid material can extend to a significant (atomistic) scale into the vapor phase, and the interface in this case has an extended area. Gibbs invented an ultrathin dividing plane as an ideal interface for the two phases. The amount of segregation is defined as interface excess Γ and it is quantified according to the position of a specific dividing interface, which is the dashed line in Figure 6.

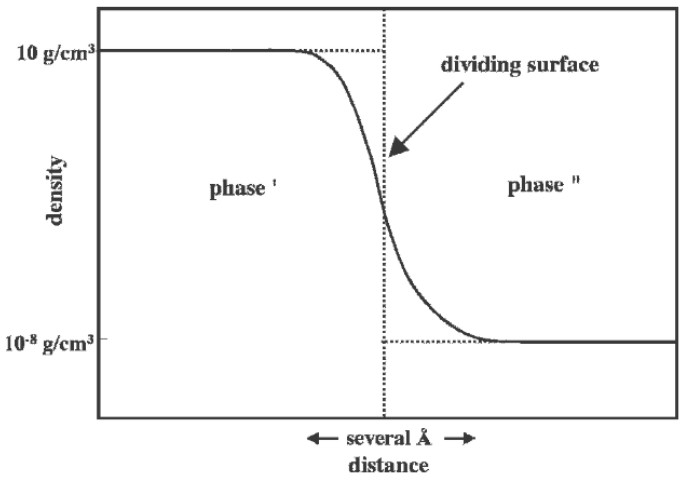

Figure 6: Schematic density variation across a solid-vapor interface[37]**.**

In Gibbs' approach the interface is ultrathin and without any volume. The internal interfacial energy, total energy excess at the surface/interface can be written as:

$$dE^{\sigma} = TdS^{\sigma} + \gamma dA + \sum_{1}^{i} \mu_i^{\sigma} dn_i^{\sigma} \tag{8}$$

where σ represents the interface, T is the temperature, S is the entropy, A is the interface area, γ is the surface or interface energy, μ_i and n_i is the chemical potential and the number of moles of component i. Integrating equation (8) results in:

$$E^{\sigma} = TS^{\sigma} + \gamma A + \sum_{1}^{i} \mu_i^{\sigma} n_i^{\sigma} \tag{9}$$

Doing a full differentiation of the above, and then subtracting equation (8) from it, we can obtain the 'Gibbs-Duhem equation' of the interface in Gibbs convention.

$$S^{\sigma} dT + Ad\gamma + \sum_{1}^{i} n_i^{\sigma} d\mu_i^{\sigma} = 0 \tag{10}$$

Defining the specific interface excess Γ as the excess of number of moles of component i per interface area results in:

$$\Gamma_i = \frac{n_i^{\sigma}}{A} \tag{11}$$

Together with (10)：

$$d\gamma = -s^{\sigma} dT - \sum_{1}^{i} \Gamma_i^{\sigma} d\mu_i^{\sigma} \tag{12}$$

At constant temperature $dT = 0$, we can obtain the **Gibbs adsorption isotherm**:

$$d\gamma = -\sum_{1}^{i} \Gamma_i \, d\mu_i \tag{13}$$

Generally speaking, the isotherm indicates that if positive excess of one chemical component is found at the interface, with increasing chemical activity of this component in the bulk phase, it will contribute to a decrease in the interface energy. Consider a two-component system, solute B in solvent A, for dilute solution (c for atomic concentration, k is the Boltzman constant) [25]. If we can define a dividing interface to make interface excess of solvent A to be zero:

$$\mu_B = \mu_B^{\circ} + kT \ln c_B \tag{14}$$

$$\frac{d\gamma}{d\mu_B} = -\Gamma_{B(\Gamma_A=0)} = -\Gamma_{B(A)} \tag{15}$$

Combining (14) and (15):

$$d\gamma = -kT \frac{\Gamma_B(c_B)}{c_B} dc_B \tag{16}$$

Since the concentration is a measurable property, if the relation of excess according to concentration is known, the change in interface/surface energy due to adsorption/segregation can be integrated from Equation (16).

1.3 Dewetting of Thin Films

1.3.1 Solid and Liquid State Dewetting

Dewetting is a term used to describe the inverse process of liquid spreading on solids. Dewetting of thin films is a shape evolution driven by capillary forces. Thin films are known to be in a metastable state and have the tendency to break up and agglomerate to islands of materials. From a thermodynamic point of view, the driving force of dewetting stems from the reduction of total energy, which includes surface energy of the thin film as well as the substrate, and the interface energy between the film and the substrate. While dewetting can be catastrophic for some electronic device systems, it has been applied to produce defined arrays of nanoparticles or structures in catalysts [38,39], sensors [40] and memory devices [41].

Experimental and theoretical modeling to understand the dewetting process have been investigated for decades. Dewetting can be divided into two scenarios. One is liquid-state dewetting where the thin film will be brought to a liquid state and the driving force for rupture of the thin film is caused by Rayleigh instability due to a thermally activated wave fluctuation through the film [42]. The other is solid-state dewetting, where the film is kept in a solid state throughout the whole process. For a thin solid film with a flat and energetically isotropic surface, if the surface diffusion perturbations are smaller than the

film thickness, the film will be (kinetically) stable [43]. In this condition of solid state dewetting, void nucleation in the film plays an important role as a necessary precursor for film rupture [44, 45].

For solid-state dewetting of polycrystalline films, the initial stage starts from grain boundaries or triple junctions where three grains meet [44,46,47]. Both grooving along the grain boundaries from the free surface to the substrate, and nucleation of voids at the film-substrate interface from the substrate to the free surface, can lead to the rupture of the polycrystalline film [48]. Illustrations of these two mechanisms are shown in Figure 7.

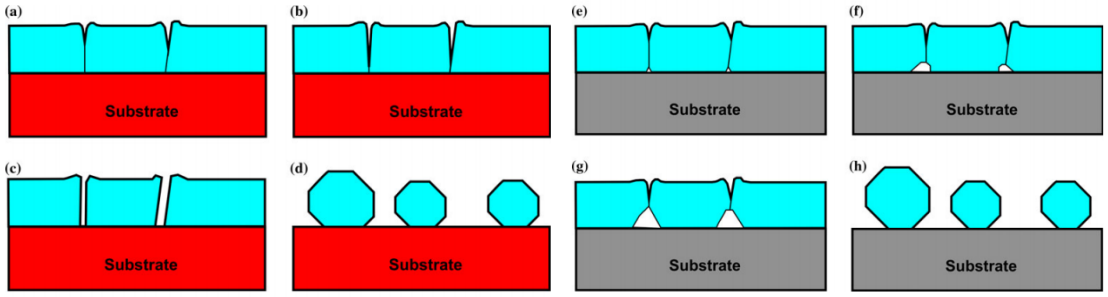

Figure 7: Schematic drawing of solid-state dewetting of polycrystalline thin film on a substrate. (a)–(d) show grain boundary grooving starting from the free surface until it hits the substrate; (e)–(h) show voids nucleation and growth towards the free surface. Illustration from [48]**.**

1.3.2 Shape Evolution of Solid Particles

After complete break-up of the thin film, islands of material will form on the substrate, and shape evolution of the islands will continue until they reach an equilibrium state. For islands in the solid state, shape evolution is facilitated by surface diffusion and driven by surface energy excess minimization.

Nichols and Mullings proposed a model for equilibration of a solid sphere under surface diffusion [49]. It should be noted that this model was developed by assuming surface diffusion as spherical harmonic perturbation along the radius direction of the solid sphere. The time for this volume-conserving equilibration process, which is the time until the completion of the perturbation along the radius of the sphere, can be written as:

$$\tau_{eq} = \frac{r^4 kT}{24\gamma D_s \nu_{at}\ \Omega^2} \tag{17}$$

where γ is the surface energy, D_s is the surface self-diffusion coefficient (assumed to be isotropic), ν_{at} is the number of atoms per unit surface area, Ω is the atomic volume, k is Boltzmann's constant and T is the absolute temperature. The equation basically indicates that particles with a smaller radius require less time to equilibrate.

While a spherical shape can give us a general indication of the time dependence of particle evolution on size and temperature, in real dewetting experiments the particle is not a sphere, but rather a faceted solid particle or rounded liquid droplet truncated by the flat substrate, and their morphology on the substrate depends on the interface energy. In the case of a solid, facets with low surface energies usually occupy a significant percentage of the surface area. Shape evolution from the as-deposited state towards equilibration requires a change of facet area on the surface, where mass transportation in both lateral and normal directions is needed. Low-energy flat surfaces without steps or defects are known to be limited in their motion in the lateral direction, except that a new layer of atoms can form on its surface, i.e. two-dimensional nucleation [50]. For shape evolution towards equilibrium, normal motion of a facet is definitely needed. However, for non-equilibrated particles with facets larger than a critical value and without any steps or defects, the nucleation energy barrier of forming a new layer of atoms can be impossible to overcome [51,52]. Thus the non-equilibrium shape will be kinetically stable and immobile, regardless of the time scale as in the previous description for the stabilization of an ideal spherical harmonic perturbation.

1.4 Au-YSZ Interface

The Au-YSZ interface has been investigated for its application in solid oxide fuel system [53–55], sensing technology [56], and catalyst applications for low-temperature CO oxidation [57,58]. It is important to understand how the interaction between Au and YSZ can result a change in general function of the system, for example, increasing the diffusion kinetics of oxygen [59,60], and determining the catalytic activity of Au [61]. To understand this, the fundamental structure and thermodynamic properties need to be studied.

1.4.1 Gold

The equilibrium crystal shape of Au was investigated mostly on ceramic substrates from dewetting experiments [62–66]. General features of the ECS of Au include facet planes from {111} and {100} families connected by rounded surfaces (see Figure 8). A comparison of the surface energy anisotropy ($\gamma_{\{100\}}/\gamma_{\{111\}}$) found in the literature is shown in Table 1. The difference in morphology or surface energy might due to a difference in temperature, equilibration atmosphere, and most importantly surface segregation of impurities. The only chemical composition characterization of the obtained equilibrated Au was done for the case of Au on α-SiC and no evidence of contaminants on the surface or bulk were claimed to have been found [62]. For Au on graphite, it was later proved that the Au particle surface can be altered with C, and as a result the surface energy anisotropy may change due to contamination [67]. The energy anisotropy in case (c) and (d) in Table 1 seem to have perfect agreement regardless of the temperature, but it should be noted that the anisotropy obtained in case (d) is from fitting a *simulated* Wulff shape to the TEM morphology of a real equilibrated Au particle. So the agreement might be a coincidence. The morphology of the equilibrated Au particles in Table 1 is shown in Figure 8. For (a) and (b), having a similar value of energy anisotropy, results in a similar equilibrium surface morphology, where a truncated sphere is intersected by {111} and {100} facets. For (c) the morphology is more faceted, showing a large area of {111} and {100} facets connected with rough surfaces.

Table 1: Surface energy anisotropy between (100) and (111) of Au from literature.

Experimental System (atmosphere)	Temperature	Anisotropy $\gamma_{\{100\}}/\gamma_{\{111\}}$
(a) Equilibrated Au on α-SiC (UHV) [62,65]	900˚C	1.04
(b) Equilibrated Au on graphite (UHV) [63]	1000˚C	1.019
(c) Equilibrated Au on (1000) sapphire (air) [68]	1000˚C	1.06
(d) Equilibrated Au on (110)TiO_2 (air) [64]	500-700˚C	1.06

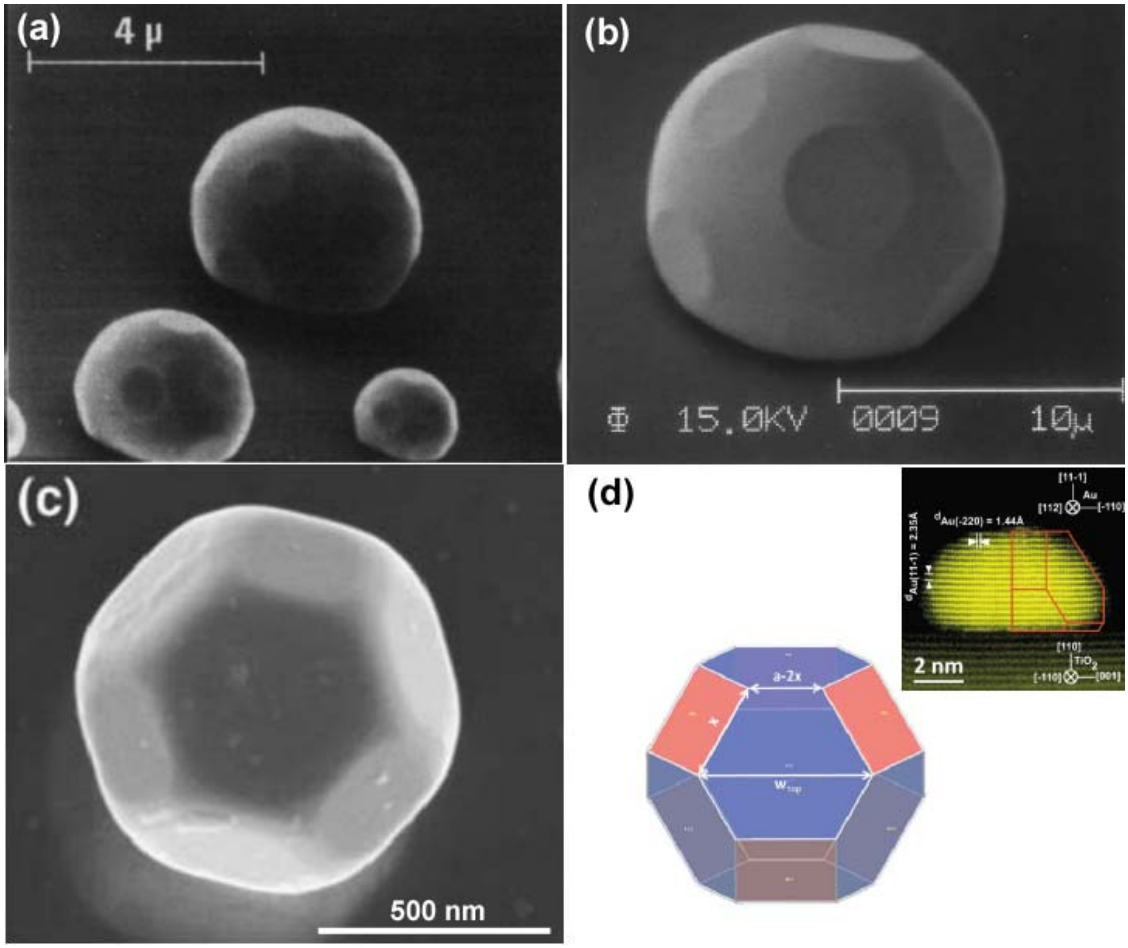

Figure 8: Equilibrium crystal shapes of gold from literature. (a) Equilibrated Au particle on graphite under UHV(1000˚C) [62,65]**; (b) Equilibrated Au on α-SiC under UHV(900˚C)** [63]**; (c) Equilibrated Au on (1000) sapphire in air(1000˚C)** [68]**; (d) Left bottom: Wulff shape of equilibrated Au on (110) TiO_2 in air(500-700˚C). The graph at the right corner is a STEM micrograph of an equilibrated Au nano-crystal on TiO_2 with a Wulff shape fitted to the Au particle** [64]**.**

1.4.2 YSZ

Pure zirconia is monoclinic at room temperature. It undergoes two structural phase transitions from the melting point to 2340°C, cubic to tetragonal, and tetragonal to monoclinic at 1170°C. However, if it is doped with a certain amount of yttria, or some other lower-valent oxides, it can be stabilized in a cubic fluorite structure at room temperature. The phase diagram of zirconia and yttria is shown in Figure 9. The addition of Y_2O_3 to zirconia stabilizes the cubic structure at room temperature through charge compensation by introducing oxygen vacancies [69,70].

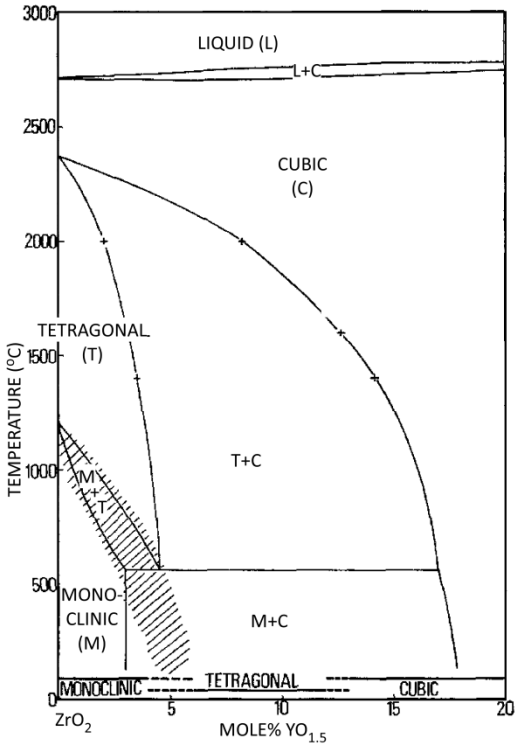

Figure 9: Phase diagram for the ZrO_2-rich part of the ZrO_2-Y_2O_3 system. The marked region indicates non-equilibrium monoclinic-tetragonal transition (redrawn after [71]**).**

2. Research Goals

The general motivation of this research was to study the influence of interfacial segregation on metal-ceramic interfaces. In this study, Au-YSZ was selected as the experimental metal-ceramic system. The main goal of this study was to determine the interface energy and orientation relationship between undoped Au-YSZ interfaces, as well as the equilibrium crystal shape of Au, and to look into interface adsorption effects on interface energy and structure.

To create Au-YSZ interfaces, dewetting experiments were conducted in both the liquid and solid states.

3. Experimental Methods

In this chapter, sample preparation, dewetting experimental conditions and characterization methods will be described.

3.1 Dewetting Experiments

YSZ (111) oriented substrates (13 mol% yttria) were used in this study. The 99.99% purity substrates were provided by MaTech Material Technology & Crystal GmbH (Julich, Germany). Polished substrates were carefully cleaned before deposition (details will be provided below). Each sample used in the experiment was prepared by depositing a 30nm-thick Au (99.999% purity) film on the (111) YSZ substrates by either e-beam evaporation (Airco Themescal FC 1800) or sputter coating (Ardenne LS 320 S sputter system).

3.1.1 Solid-State Dewetting in a Controlled Atmosphere

Two repeated sets of solid-state dewetting were conducted for the purpose of creating clean Au-YSZ interfaces. For the first set of experiments, the YSZ substrates were cleaned with acetone, ethanol and isopropyl using an ultrasonic bath. Ca contamination was subsequently found at the Au-YSZ interfaces in samples from the first solid-state dewetting experiments. Since the contamination was suspected of coming from the cleaning process, a new cleaning procedure was conducted in the Technion clean rooms with acetone, methanol, isopropanol and deionized water in an ultrasonic bath, followed by plasma cleaning. Substrates used in both solid-state dewetting experiments were deposited with ~30nm thick Au film by e-beam evaporation deposition.

The as-deposited samples were annealed in a sapphire tube furnace at 950˚C ($0.89T_m$ of Au), in flowing Ar + 7 vol. % H_2 (99.9999% pure) at an oxygen partial pressure of P (O_2) = 10^{-20} atm for 48 h. The annealing process was done in a dedicated tube system made up of five 99.99% purity single-crystal sapphire tubes to prevent sample contamination (see Figure 10). The partial pressure of oxygen was measured at the exit

port of the sapphire tube furnace using a zirconia oxygen detector (Rapidox 2000 oxygen analyzer, Cambridge Sensotec).

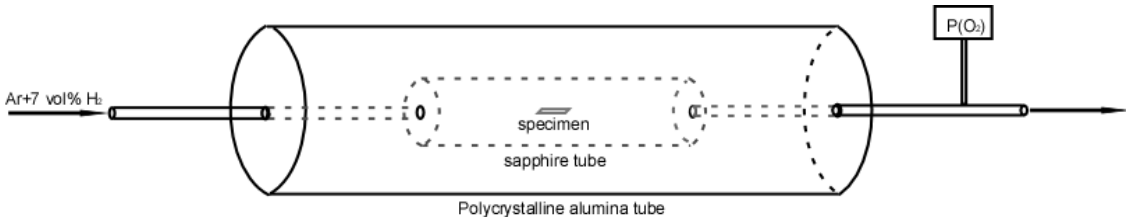

Figure 10: Schematic drawing of the sapphire tube furnace used for the dewetting experiments.

3.1.2 Liquid and Solid State Dewetting in Air

Dewetting experiments were also conducted in air. For these experiments, the same (111) YSZ substrates were used and cleaned with acetone, ethanol and isopropyl using an ultrasonic bath before deposition of Au. As-deposited samples were prepared by sputter coating (Ardenne LS 320 S sputter system) with an expected thickness of 30 nm.

For the solid-state dewetting experiments, the annealing temperature was set to 960℃ ($0.90T_m$ of Au) for a period of 24 hours. For liquid-state dewetting experiments, the temperature was first raised to 1100℃ (above the T_m of Au) for 30 minutes and then cooled to 1000℃ ($0.94T_m$) for 48 hours of equilibration.

3.2 TEM Sample Preparation

As will described in the following Results section, a large quantity of submicron Au particles form on the YSZ substrate, but not all of these particles reached equilibrium. Since in this study only the equilibrated particles are of interest, site-specific TEM samples were produced from selected particles using a dual-beam FIB (Strata 400s, and FEI Helios NanoLab Dual Beam G3 UC, FEI, Eindhoven, the Netherlands), using the in-situ "lift-out" technique (see Figure 11) [72–74].

Equilibrated particles were selected according to their symmetry in shape (see Figure 11 (a)). Selected particles were coated with C and Pt to protect the surface morphology from the Ga ion beam. All the particles were aligned to a certain direction according to their facets, in order to prepare a TEM lamella of the Au-YSZ interface with the Au particle already aligned *near* to the [110] zone axis. After a trench was cut by ion milling (Figure 11 (b)), and a "U-cut" was made under the lamella, the lamella was joined to a micromanipulator needle using Pt deposition (Figure 11 (c)). After removing the lamella from the substrate, it was attached to a TEM grid, and subsequently polished to electron transparency (Figure 11 (f)).

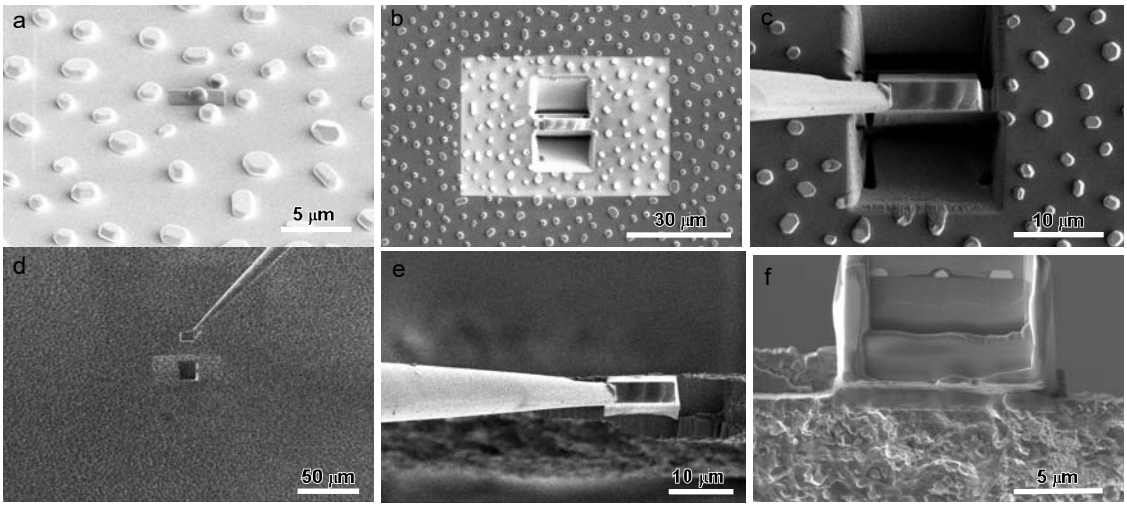

Figure 11: Illustration of FIB in-situ lift-out process: (a) A selected equilibrated gold particle is marked and protected with carbon deposition; (b) A "U-cut" is made by gallium ion milling at both side of the selected the particle; (c) A needle is attached to the lamella; (d) Lift-out of the lamella; and (e) The lamella is attached to a TEM grid followed by (f) thinning of the lamella.

3.3 SEM and TEM Characterization

3.3.1 Characterization and Simulation of Au Morphology

The surface morphology of the dewetted Au particles on YSZ substrates was characterized using HRSEM (Zeiss Ultra-Plus FEG-SEM). Cross-section TEM characterization was conducted using a FEI Tecnai G2 T20 S-Twin S/TEM.

Simulation of the equilibrated Au particle shape was done using the open source "Wulffmaker" software [75], where the space group, number and index of facet families,

and values of surface energies of specific planes can be manually set in order to generate an ECS.

3.3.2 Orientation Relationship Characterization

3.3.2.1 Electron Back Scattered Diffraction

Statistics of the orientation relationships between equilibrated Au particles and YSZ substrates was obtained using EBSD (Oxford instruments, UK) mounted on a SEM (Zeiss Ultra-Plus FEG-SEM). Analysis of the EBSD data was conducted using MTEX free MATLAB tool box.

3.3.2.2 X-Ray Diffraction θ-2θ Technique

Preferred orientation of the as-deposited and dewetted Au on (111) YSZ was determined using X-ray diffraction (XRD), with Cu-Kα radiation operated at 45 kV and 150 mA (Xray: Rikagu Smart Lab X-Ray Diffractometer). A θ-2θ parallel beam geometry with a Ge(220)×2 monochromator was used for analysis of the integrated intensities of the Au reflections.

The basic set-up for diffractometer is shown in Figure 12. In the θ-2θ operation, the X-ray tube is fixed while the sample and detector rotates. The sample rotates at θ°/min and the detector rotates at 2θ°/min. The substrates surface vector **s** were accurately aligned in the chamber by rocking curve pre-measurements according to the Bragg angle of the (111) reflection of the YSZ substrate. Recognition of (111) reflection of YSZ was done by referring to the powder diffraction card of $Y_{0.15}Zr_{0.85}O_{1.93}$ from International Center for Diffraction Data (ICDD) [76].

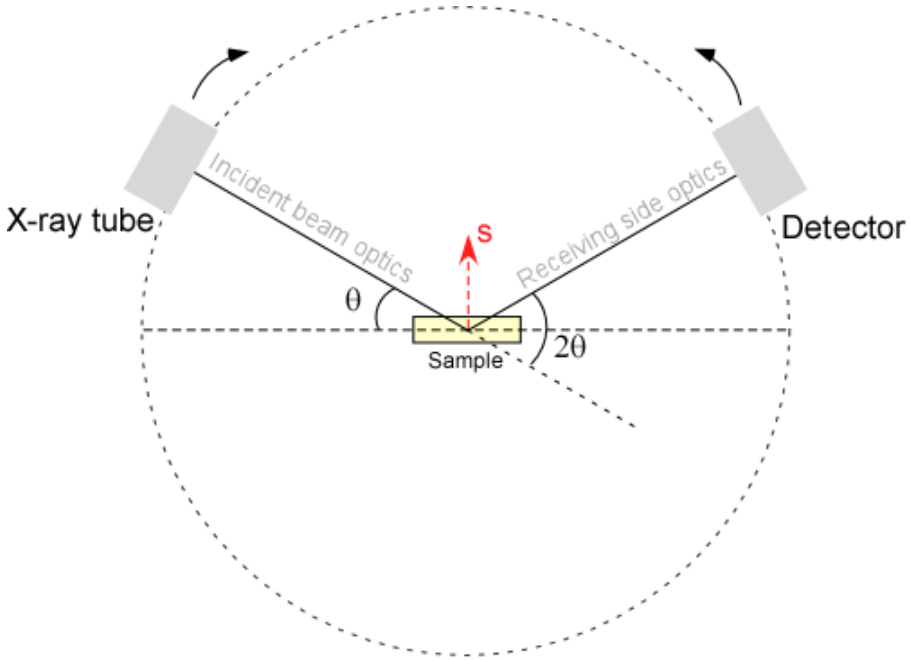

Figure 12: Illustration for basic set-up of a diffractometer. X-ray tube is the x-ray source.

The degree of preferred orientation was determined using the equation:

$$P_{hkl} = \frac{I_{hkl}}{I'_{hkl}} \cdot \frac{\sum I'_{hkl}}{\sum I_{hkl}} \qquad (18)$$

where I_{hkl} is the measured intensity of reflection from the hkl plane and I'_{hkl} is the random intensity. Summation is conducted over all the measured reflections.

X-ray θ-2θ characterization was conducted along with the P ratio calculation on dewetted Au particles to determine the preferred orientation of Au particles. Standard intensities of for randomly oriented Au were taken from the ICDD [77].

Table 2: Standard random intensity of Au [77]**.**

Reflection (Au)	2θ	standard intensity
111	38.18362	100
200	44.39166	25
220	64.57593	55
311	77.54709	40
222	81.72124	6
400	98.13339	5
331	110.79762	10
420	115.25934	6

3.3.3 Interface Chemistry Characterization

A monochromated and double-corrected S/TEM (Titan-Themis3 300, FEI) was used at an accelerating voltage of 300 kV in high angle annular dark field scanning transmission electron microscopy (HAADF-STEM) mode combined with EDS measurements (with an FEI Super-X detector system) to acquire elemental maps of the chemistry at the Au-YSZ equilibrated interfaces.

To determine chemical excess at the interface, the spatial difference technique was used [78,79]. The interfacial intensity of a segregated species is given by:

$$I_s = I_{int} - \tfrac{1}{2}(I_{bulk\,A} + I_{bulk\,B}) \qquad (19)$$

As indicated from Equation (19), in order to do spatial difference analysis, EDS spectrum need to be acquired from three different areas (see Figure 13); two from the Au and YSZ bulk phases away from the interface, and one from the interface area with a width that is enough to cover the interfacial segregation layer. If we extract the intensity

of bulk Au and bulk YSZ from the interface spectrum, the remaining intensity will be the intensity from the chemical excess at the interface.

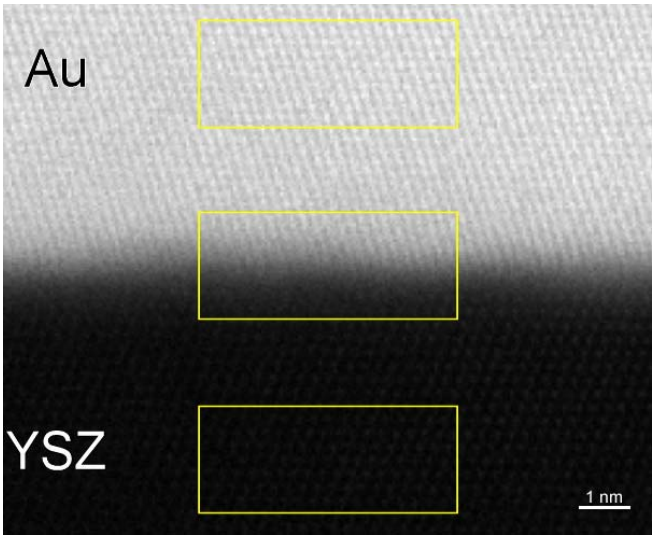

Figure 13: Areas of EDS acquisition for spatial difference.

4. Results

The results are divided into two parts. First, results from two repeated solid state dewetting experiments in a controlled atmosphere are presented, as well as the simulation of the Au ECS, the measured interface energy, the orientation relationship and interface chemistry. Following this, results regarding the morphology and preferred orientation from solid and liquid dewetting in air are shown in the second part.

4.1 Solid-State Dewetting in a Controlled Atmosphere

4.1.1 Initial Solid-State Dewetting Experiments

4.1.1.1 Morphology after Dewetting

A representative SEM micrograph of the morphology after solid state dewetting is shown in Figure 14. Most of the particles are single crystals, and only a small amount are have grain boundaries. General morphologies of dewetted particles show that not all the particles are symmetrical in shape, which means that not all of them are equilibrated. However, all of them have an upper facet that is parallel to the substrate and with 3-fold symmetry in the sequence of the facets at the side. This indicates that the top facet belongs to the {111} family of planes. This is corroborated by XRD in the following.

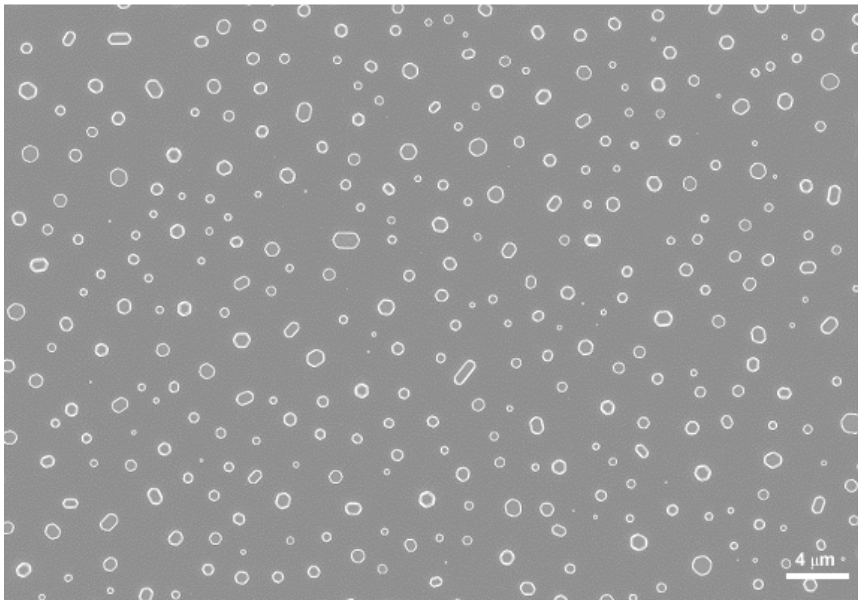

Figure 14: Sample surface morphology after dewetting at 950˚C under flowing Ar + 7vol.% H_2 for 48 hours.

Equilibrium Au particles after solid state dewetting generally have a three-fold symmetry when imaged in plan-view. The uppermost facet and the three other facet planes at the sides (indicated with arrows in Figure 15) are parallel to the {111} plane. Other than the {111} facet planes, three other facets at the side are from the {100} family of planes. The surface of the equilibrated Au particles are generally smooth. No obvious steps are visible at the edge of the {111} and {100} facet planes. Facets from the two families are connected by rounded surfaces.

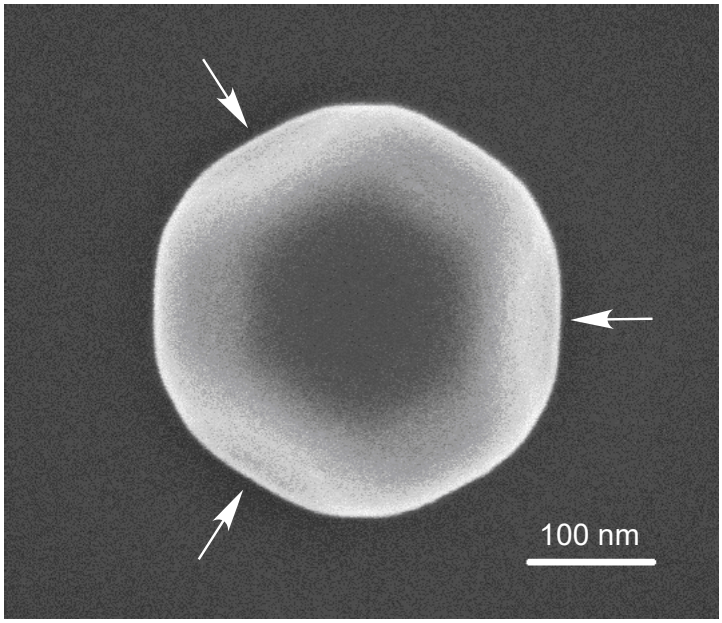

Figure 15: Secondary electron HRSEM micrograph of an equilibrated Au particle after solid state dewetting, which was equilibrated at 950˚C under flowing Ar + 7vol.% H_2 for 48 hours.

Non-equilibrated single-crystal particles can be divided into two categories: elongated (Figure 16(a)) and equi-axed with unbalanced facet planes (Figure 16(b)). In both cases, visible steps can be seen at the edge of the {111} and {100} facet planes. Clearer indication of these steps is shown in Figure 17, where a step on the {111} uppermost facet plane is marked with an arrow. This is another sign that these particles are not equilibrated.

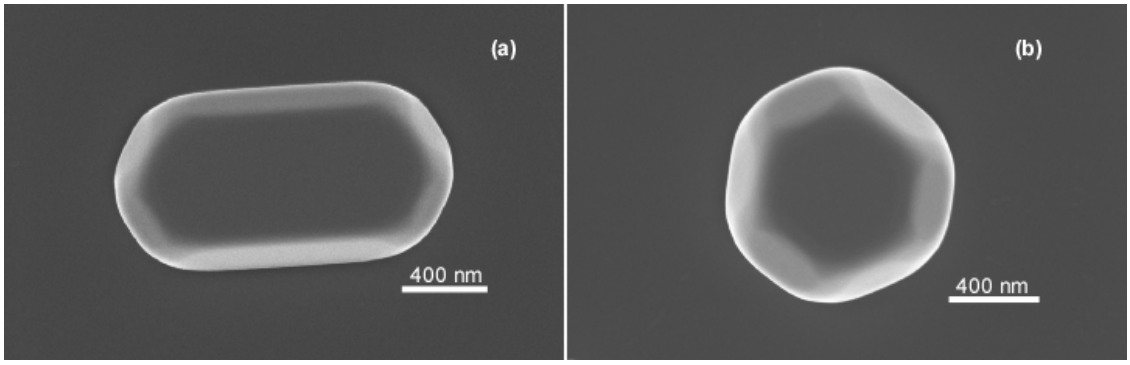

Figure 16: SEM micrographs showing representative morphologies of non-equilibrated particles. (a) An elongated non-equilibrated Au particle; (b) Equi-axed Au particle with unbalanced facet area for the {111} family of planes.

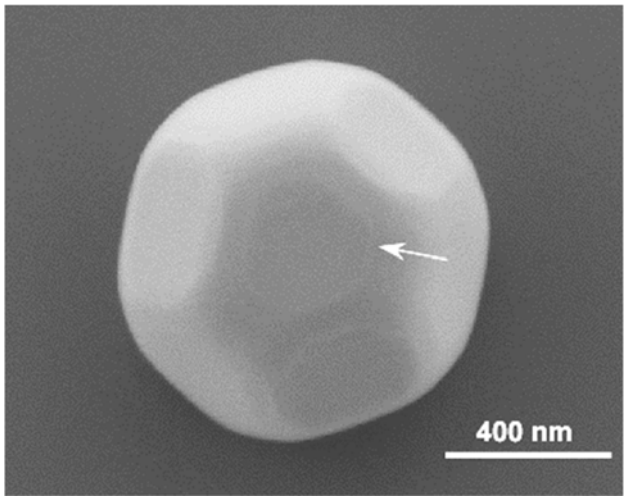

Figure 17: Secondary electron micrograph showing a sharp edge around the facets

4.1.1.2 Gold Equilibrium Crystal Shape (Simulation vs Experiment)

The Wulffmaker software was used to simulate the equilibrium crystal shape of gold [75]. Values for different surface energies were used in the simulation in order to fit the simulated shape to the result from experiments. As we can see from the experimental result, except for the {111} facets, which are the top facet and the three others at the side and the three {100} facets at the side, the particle contains rounded surfaces. So in the simulation, facets at the position of the rounded surfaces were set to a similar surface energy and are colored in grey.

The relative surface energies used in the simulation are compared to the measured values from experiment in Table 3, using an inverse Wulff construction (morphology analysis from 4.1.1.5).

Table 3: Comparison of relative surface energies $\gamma_{\{hkl\}}/\gamma_{\{111\}}$ between simulation and experiment.

	$\gamma_{\{100\}}/\gamma_{\{111\}}$	$\gamma_{\{110\}}/\gamma_{\{111\}}$
Wulffmaker	1.091	1.125
Experiment	1.067	1.116

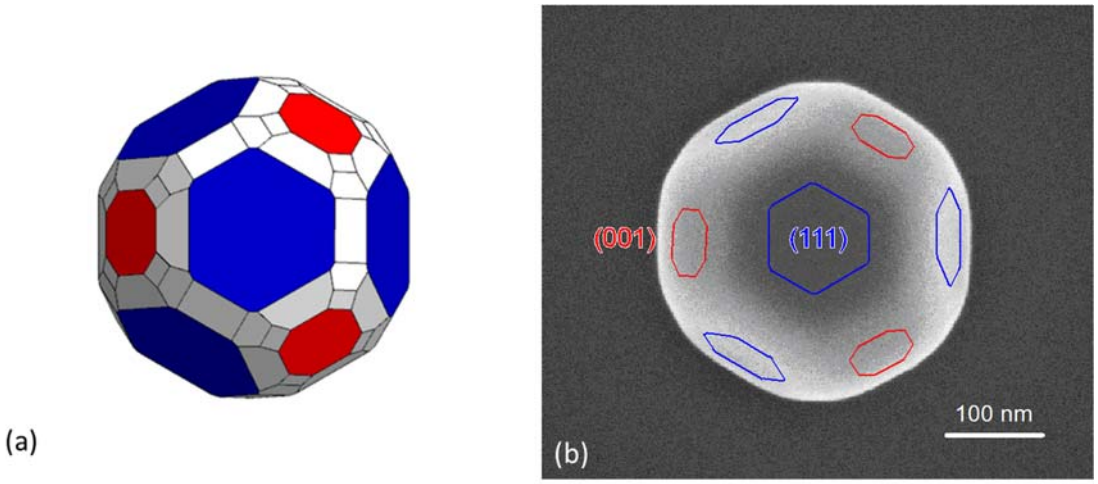

Figure 18: (a) Wulffmaker simulation of the gold equilibrium crystal shape according to the experiment results. (b) HRSEM graph of an equilibrated gold particle from solid state dewetting.

4.1.1.3 Preferred Orientation of Au on YSZ

To verify the high coincidence of facet symmetry of dewetted particles, further θ-2θ XRD characterization was conducted to determine their preferred orientation, i.e. orientation of the gold particle facet that is parallel to the YSZ substrate. XRD was also conducted on the as-deposited samples to see if there is any change in preferred orientation before and after dewetting.

Both samples were scanned in a 2θ range from 20° to 85°. XRD patterns of both samples generally include signals from the gold particles/film on the substrate and the single crystal YSZ substrate. Results from a dewetted sample shown in Figure 19 indicate that there is a strong preferred orientation of Au {111} || YSZ {111}.

P ratio analysis results showed that in both of the dewetted and as-deposited sample, the preferred orientation of Au {111} || YSZ {111} is strongly preferred. From the value of the P ratio of {111} reflections in both cases, it can be concluded that the preferred orientation exists before and after solid state dewetting and does not change significantly.

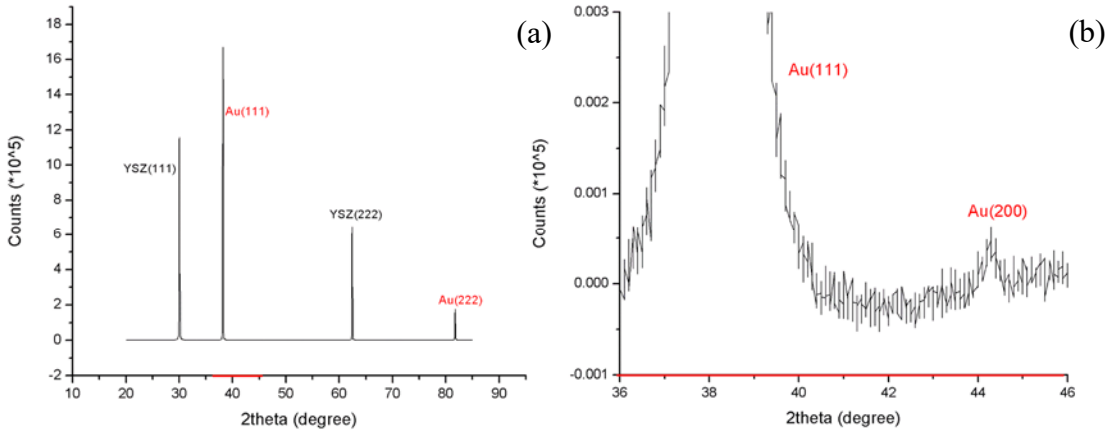

Figure 19: XRD patterns from a sample after dewetting, where (b) is a magnified angular range compared to (a).

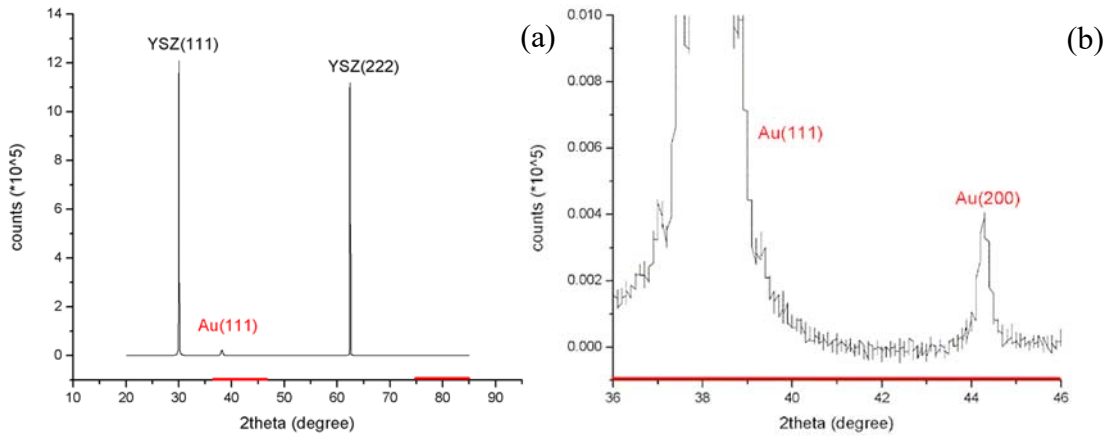

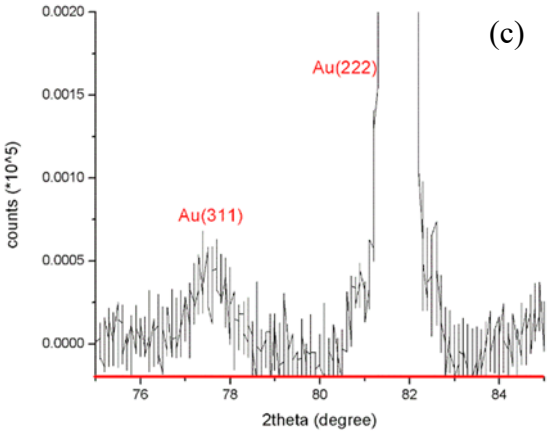

Figure 20: XRD from an as-deposited sample, where (b) and (c) are two magnified angular ranges compared to (a).

Table 4: P ratio results from dewetted and as-deposited gold.

Reflection (Au)	2θ	Measured intensity (normalized)	Standard intensity	P (dewetted)	P (as-deposited)
111	38.18	100	100	2.88	2.83
200	44.39	1.36	52	$2.2*10^{-4}$	0.07
311	77.55	0.34	36	--	0.03

4.1.1.4 Orientation Relationship of Equilibrated Au on YSZ

To characterize the potential orientation relationships of equilibrated Au particles on YSZ, site-specific EBSD characterization was conducted on 150 equilibrated particles, by manually applying scanning masks on each of the particles' upper most facets. In order to exclude the size effect of the EBSD mask on the signal from different sized equilibrated particles, one set of Euler angles that represents the orientation of the particle was extracted from the mask and replotted using the MTEX tool box in

MATLAB. The results are shown in Figure 21. The results of this analysis indicate that there is no low-index orientation relationship of the equilibrated particles with the substrate, but rather a strong preferred orientation of Au {111} || YSZ {111}.

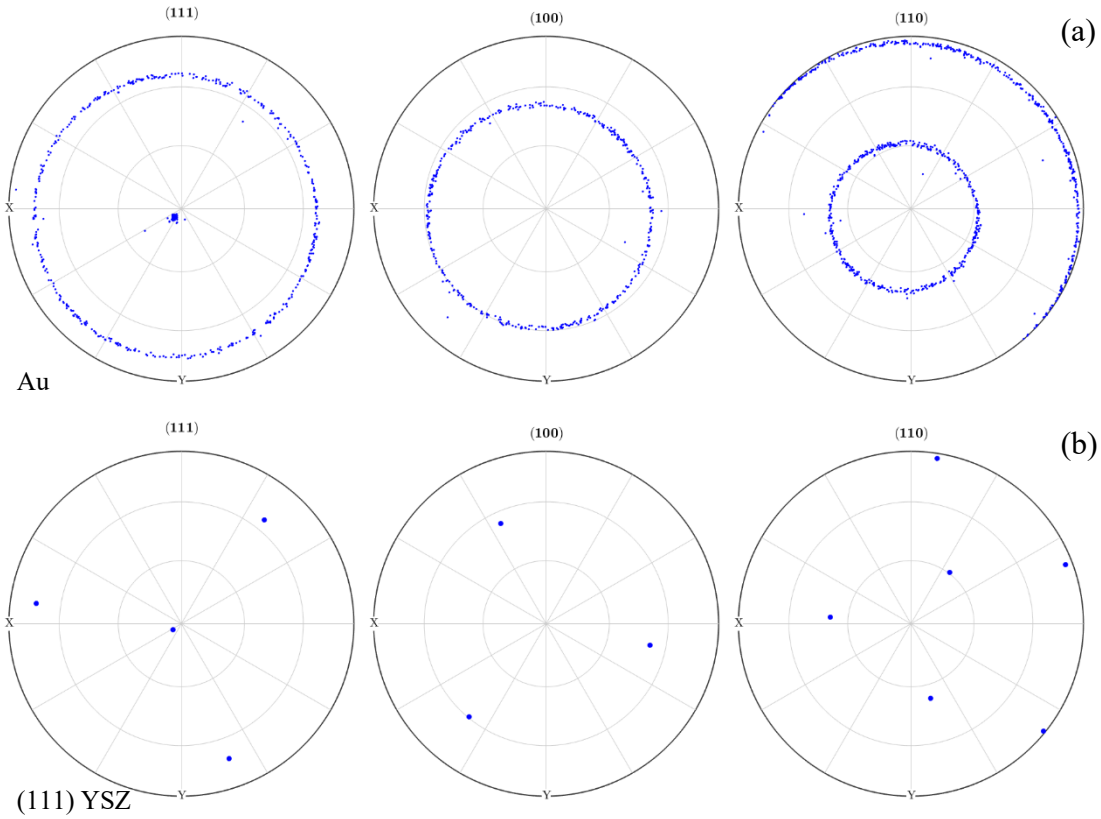

Figure 21: EBSD orientation relationship results of equilibrated Au particles on (111) YSZ. (a) EBSD pole figures in 3 different pole directions for 150 equilibrated gold particles from the first solid-state dewetting; (b) orientation of (111) YSZ substrate.

4.1.1.5 Interface Energy and Chemistry

Three Au particles with different in-plane orientations were prepared using FIB and characterized by TEM. Bright field micrographs and selected area diffraction patterns are shown in Figure 22. Only one of the particles (c) is in a low-index orientation relationship with the substrate, which is Au $[\bar{1}10](111) \parallel$ YSZ $[1\bar{1}0](111)$. The other two are in high-index orientation relationships that cannot be deciphered, but their in-plane rotations about the <111> direction of the substrate/particle are different. This was confirmed by SEM before FIB sample preparation. In all three cases the interface was found to be flat and co-planar with the substrate surface.

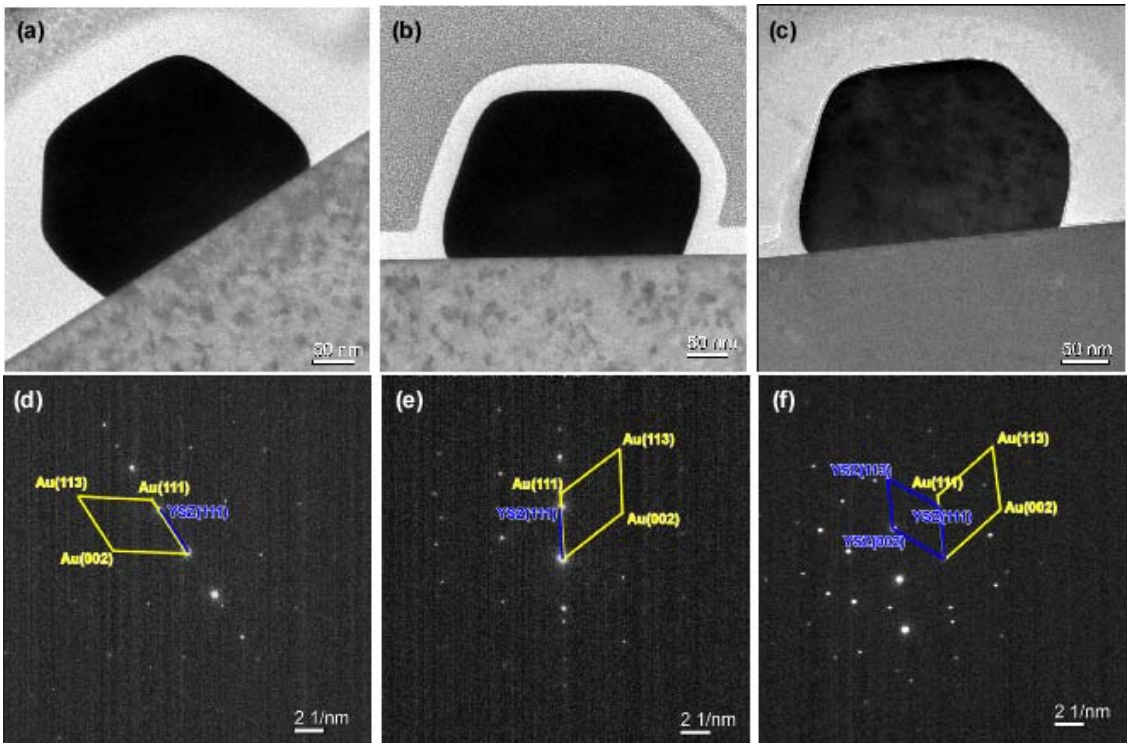

Figure 22: (a) (b) (c) Bright field TEM image of three equilibrated gold particles (black area) along with parts of the YSZ substrate. (d) (e) (f) Selected area diffraction patterns taken from the Au-YSZ interface region. Reflections from Au particles are marked in yellow, and reflections from YSZ are marked in blue. Both the BF micrographs and diffraction patterns were acquired after aligning the particle to $[\bar{1}10]$ zone axis.

Interface energy measurements were done on all the three equilibrated Au particles using Winterbottom analysis. The distances from the Wulff center of the particles to the interface R_1 and to the (111) facet plane of the particles R_2 were measured (see Figure

23) and used in Equation 7 to determine the interface energy. The surface energy of the (111) Au plane was taken as 1.4 J/m^2 from [5]. The surface energy of (111) YSZ was taken as 1.17 J/m^2 from [80]. As indicated in the BF micrographs, the interface plane is co-planar with the substrate surface, which means no residual error because of deviation of the interface plane. The results are shown in Table 5.

Table 5: Interface energy results from particle (a), (b) and (c). See Figure 22.

Particle	(a)	(b)	(c)
Interface energy(J/m^2)	1.74	1.74	1.78

The average interface energy from the three particles in Table 5 is **1.75 ± 0.02 J/m^2**.

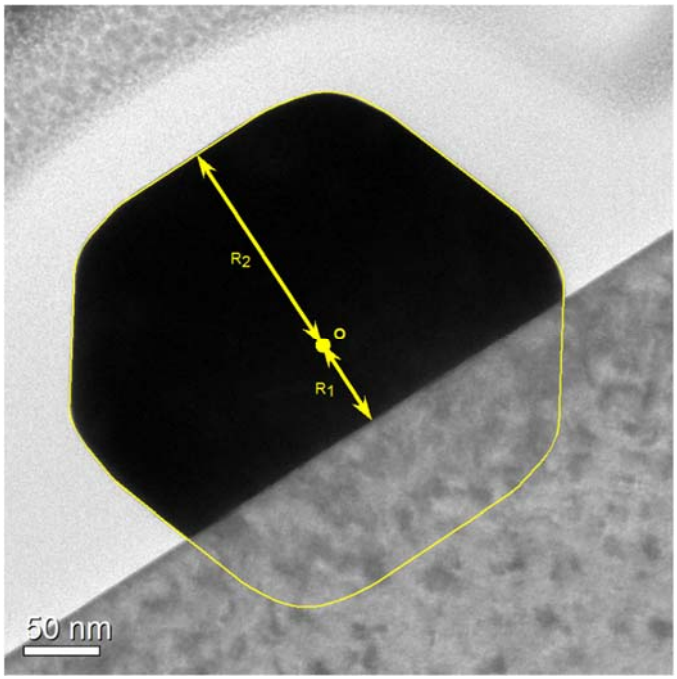

Figure 23: Winterbottom analysis of an equilibrated Au particle. The yellow outline is the Wulff shape of the Au crystal. The distance from the Wulff center to the interface and uppermost (111) facet of Au are marked as R_1 and R_2, respectively.

Chemical characterization of the Au-YSZ interface from particle (c) in Figure 22 was conducted using HAADF STEM combined with EDS elemental mapping. The Au particle was aligned into a [110] zone axis in order for the interface to be parallel to the incident electron beam (edge-on). Clear evidence of Ca segregation is shown in Figure 24, confirmed by quantitative line-scans across the interface (Figure 25). Spatial

difference spectrum acquired from the interface region, from the bulk Au, and from the bulk YSZ are shown in Figure 26. Comparison of the Ca signal from the three regions in Figure 26 (b) further confirmed a Ca excess at the interface. EDS characterization was also conducted at the (111) Au surface. The results in Figure 27 show no detectable Ca segregation at the (111) Au free surface. Due to the large solid angle of the EDS detectors mounted in the system, as well as the scattering nature of x-rays, non-local X-ray signals from the TEM pole-piece are detected. For this reason, signals of Fe, Ti and Mo are shown in the spectrums. The latter two (Ti and Mo) are from the TEM grid used for the specimen.

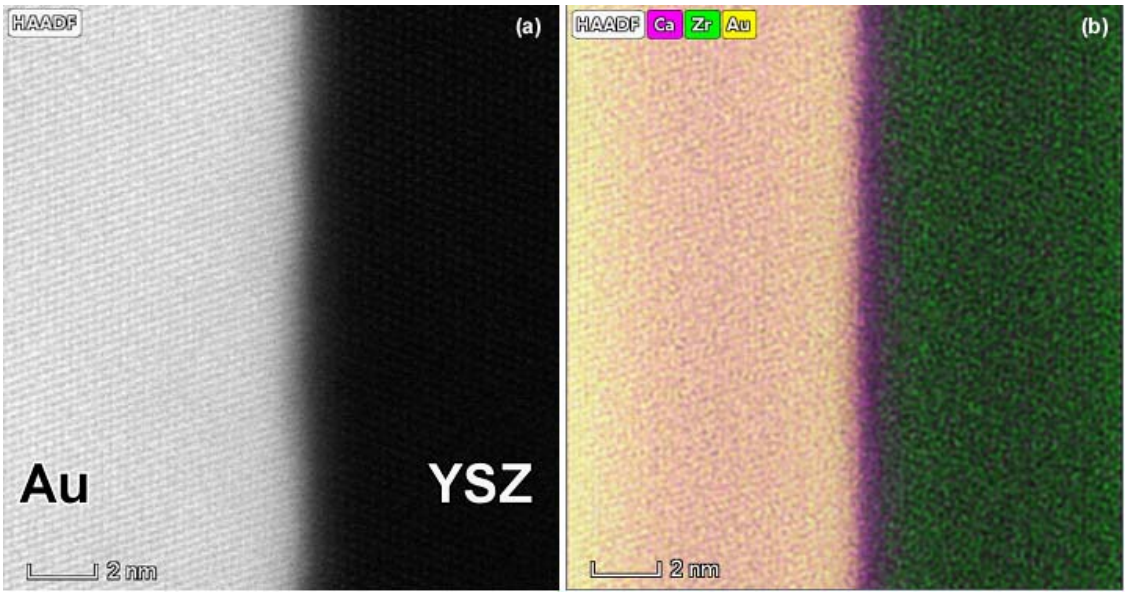

Figure 24: (a) HAADF STEM micrographs of the interface of particle (c) in Figure 22. (b) HAADF STEM micrograph combined with EDS elemental mapping showing Ca segregation colored in purple at the interface.

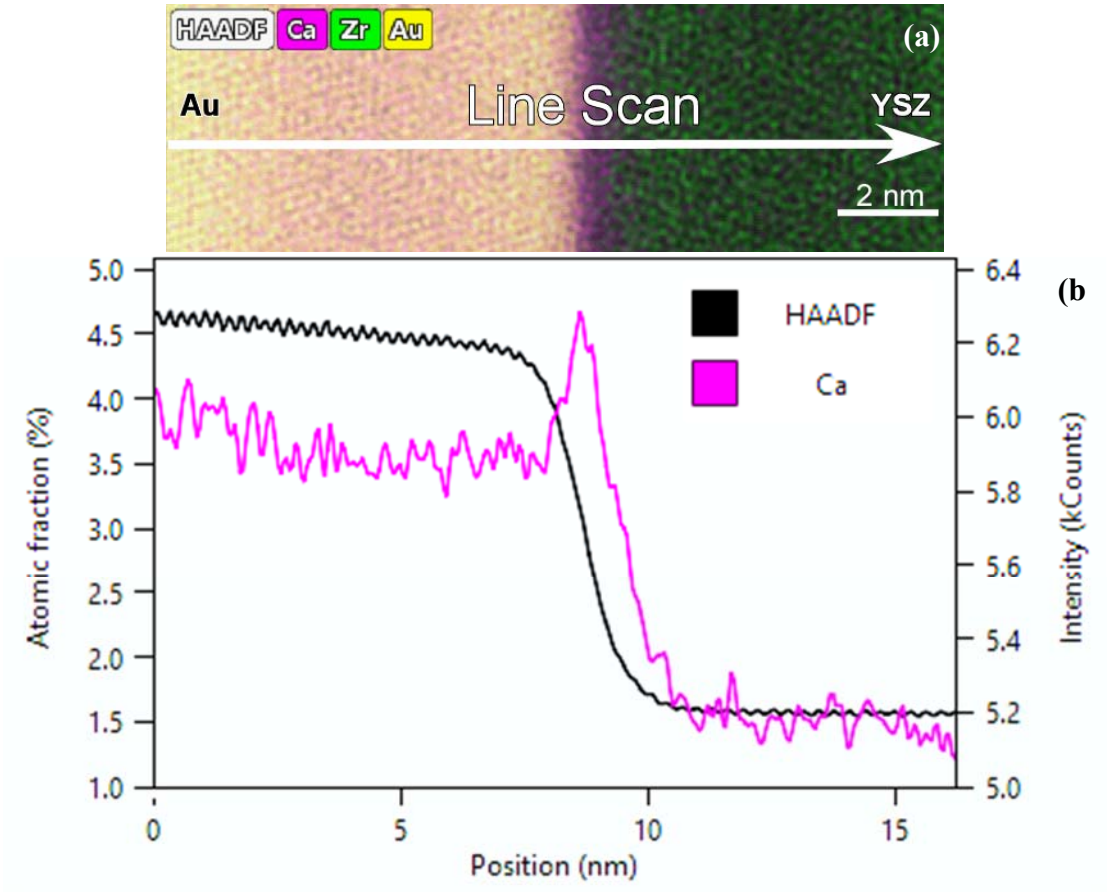

Figure 25: (a) The region from which an EDS line-scan across the interface was acquired. (b) EDS line-scan data showing an excess of Ca at the interface.

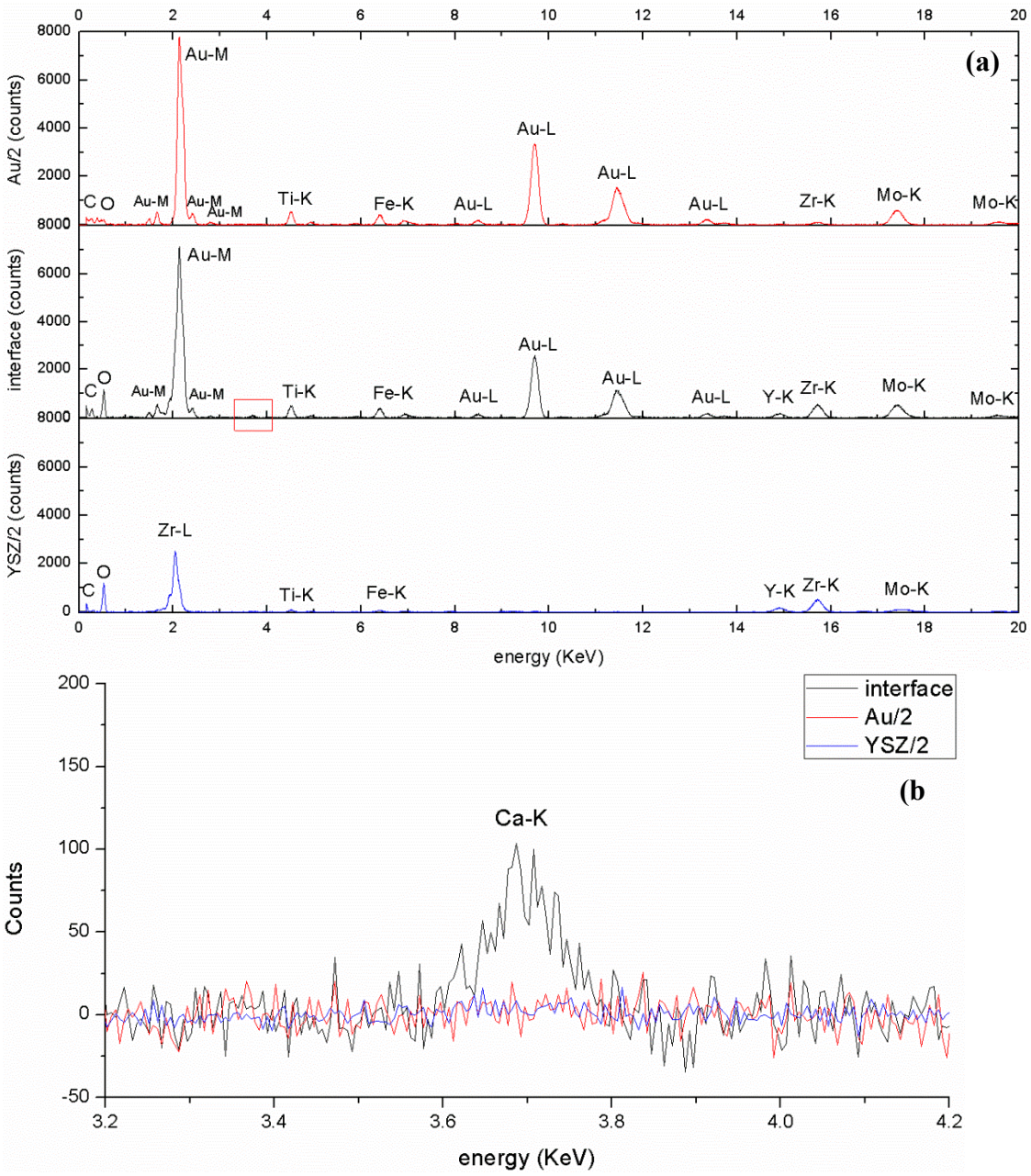

Figure 26: Spatial difference analysis of a Au-YSZ interface. (a) Uppermost spectrum in red is the EDS spectra from half of the EDS scanning box in the Au particle. The spectrum in the middle in black is the EDS spectra acquired from the interface region (the red square in the spectra marks the Ca peak). The spectra at the bottom is from half of the scan-box in the YSZ substrate. (b) Magnified Ca peak from the Au, interface, and YSZ, showing the clear existence of Ca exess at the interface.

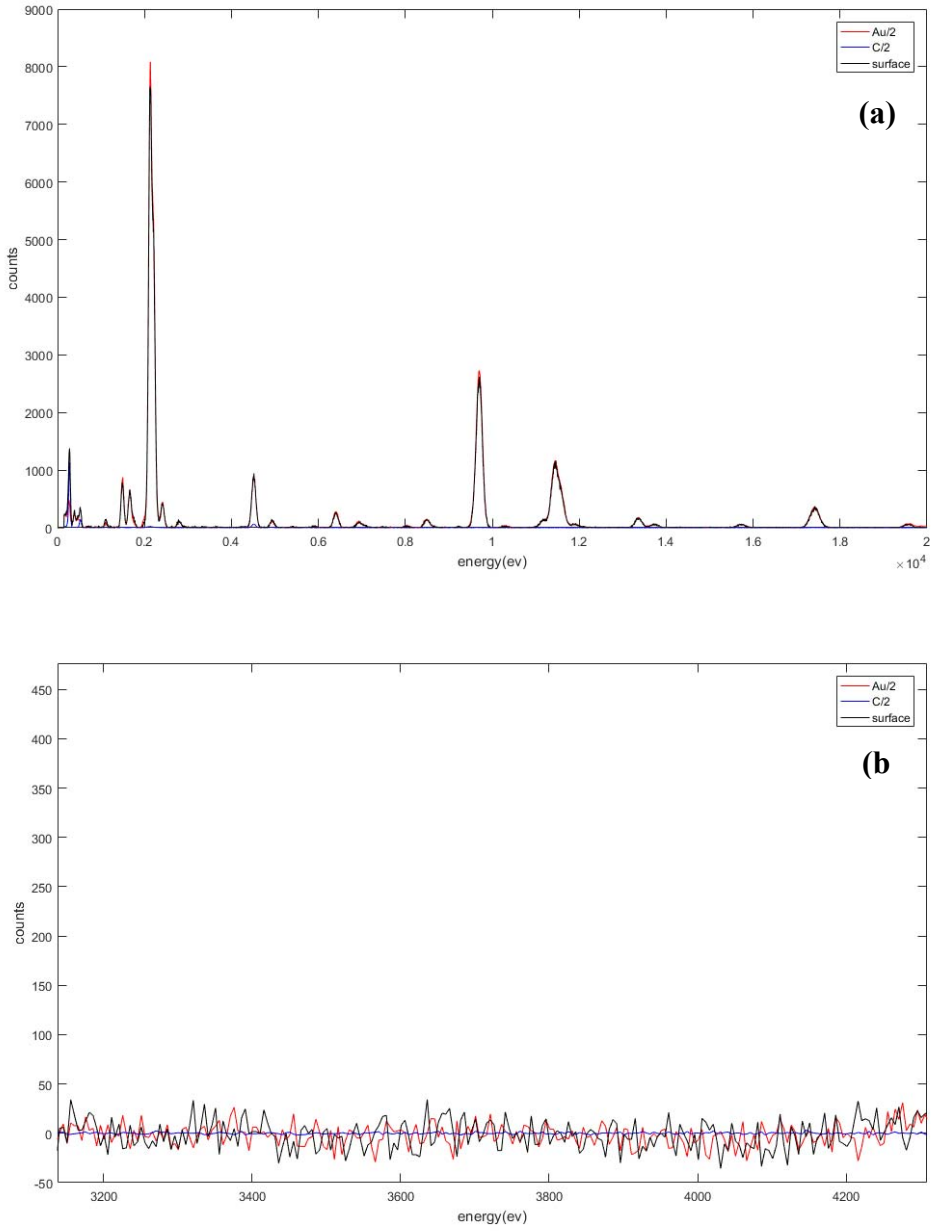

Figure 27: Spatial difference spectrum from the (111) Au free surface. (a) presents the three EDS spectrum from Au bulk, (111) Au surface area, and the carbon layer next to the (111) Au surface. (b) is the magnified segment from (a) showing no Ca excess on the (111) surface.

4.1.2 Second Set of Solid-State Dewetting Experiments

A second set of solid-state dewetting experiments was conducted under the same experimental conditions, after using an improved cleaning process for the substrates. The results are presented in the following.

4.1.2.1 Preferred Orientation of Au on YSZ

As deposited and solid-state dewetted samples both characterized by XRD, and in a 2θ range from 20° to 85°. The results from a dewetted sample are shown in Figure 28, indicating that there is a strong preferred orientation of Au {111} || YSZ {111}.

P ratio analysis shows that in both the dewetted (Figure 28) and as-deposited samples (Figure 29), the preferred orientation of Au {111} parallel to YSZ {111} is strongly preferred (see Table 6). From the value of the P ratio it can be concluded that the (111) preferred orientation exists before and after solid-state dewetting, and does not change significantly due to the dewetting process.

As for the preferred orientation, results of the two solid-state dewetting experiments did not change.

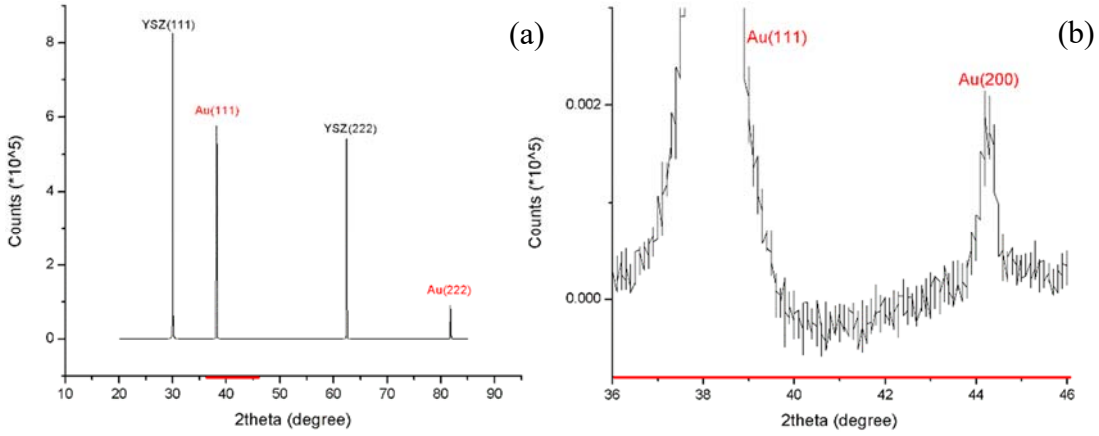

Figure 28: XRD pattern from a sample after solid-state dewetting: (a) is the full pattern acquired from 20° to 80°; (b) is a segment of (a) and only includes reflections from the gold particles.

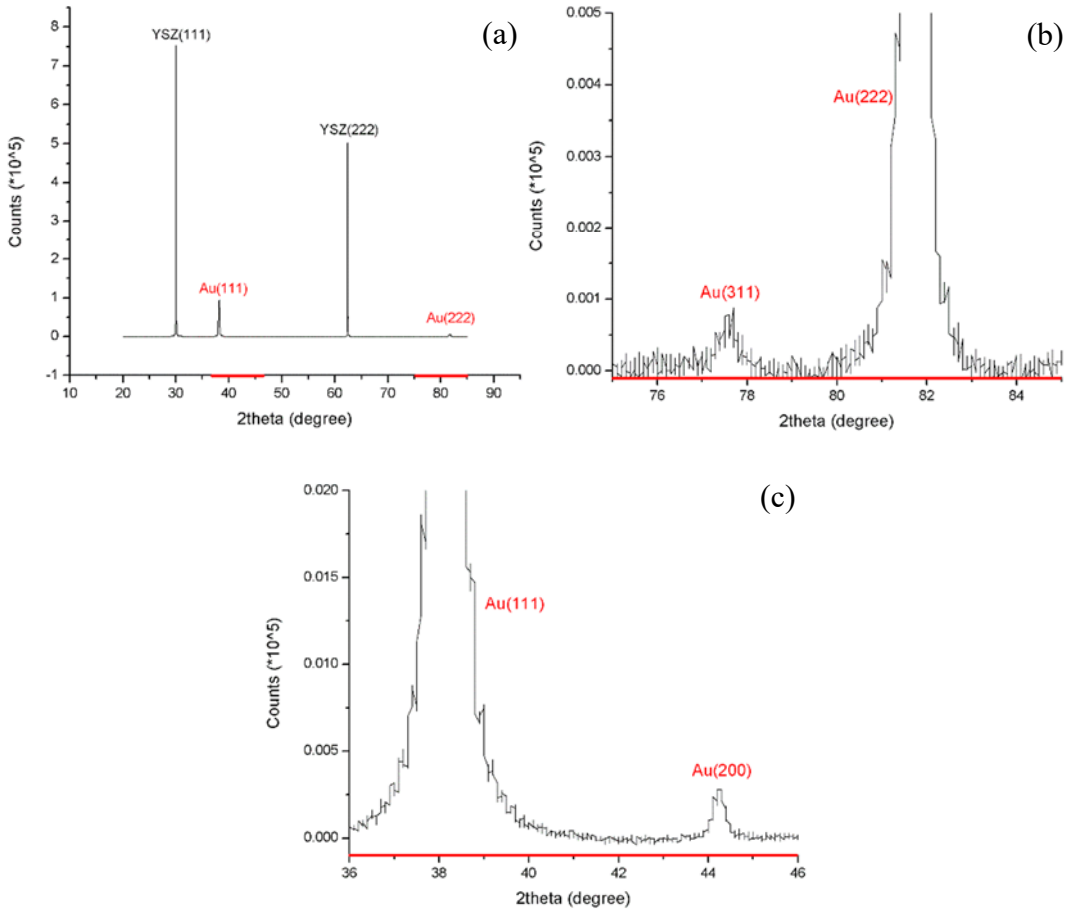

Figure 29: XRD pattern from the as-deposited sample after improved substrate cleaning. (a) Full spectrum includes signals from polycrystalline Au thin film and the single crystal (111) YSZ substrate, ranging from 20° to 80°. (b) (c) Segments of (a) that include all reflections of Au.

Table 6: P ratio results of the second solid state dewetting experiments.

Reflection (Au)	2θ	Measured intensity (normalized)	Standard intensity	P (dewetted)	P (as-deposited)
111	38.18	100	100	2.88	2.86
200	44.39	1.36	52	$5.5*10^{-3}$	0.02
311	77.55	0.34	36	--	0.01

4.1.2.2 Orientation Relationship of Equilibrated Au on YSZ

Site-specific EBSD characterization was conducted on 150 equilibrated particles from the second solid-state dewetting experiments and their Euler angles were replotted to pole figures using the MTEX tool box in MATLAB. The results are shown in Figure 30. The results of this analysis indicate that there is no low-index orientation relationship of the equilibrated particles and the substrate, but rather a strong preferred orientation of Au {111} || YSZ {111}. In comparison to the previous set of dewetting experiments (with Ca segregation), the results are the same regarding the absence of a low-index orientation relationship and the strong preferred orientation.

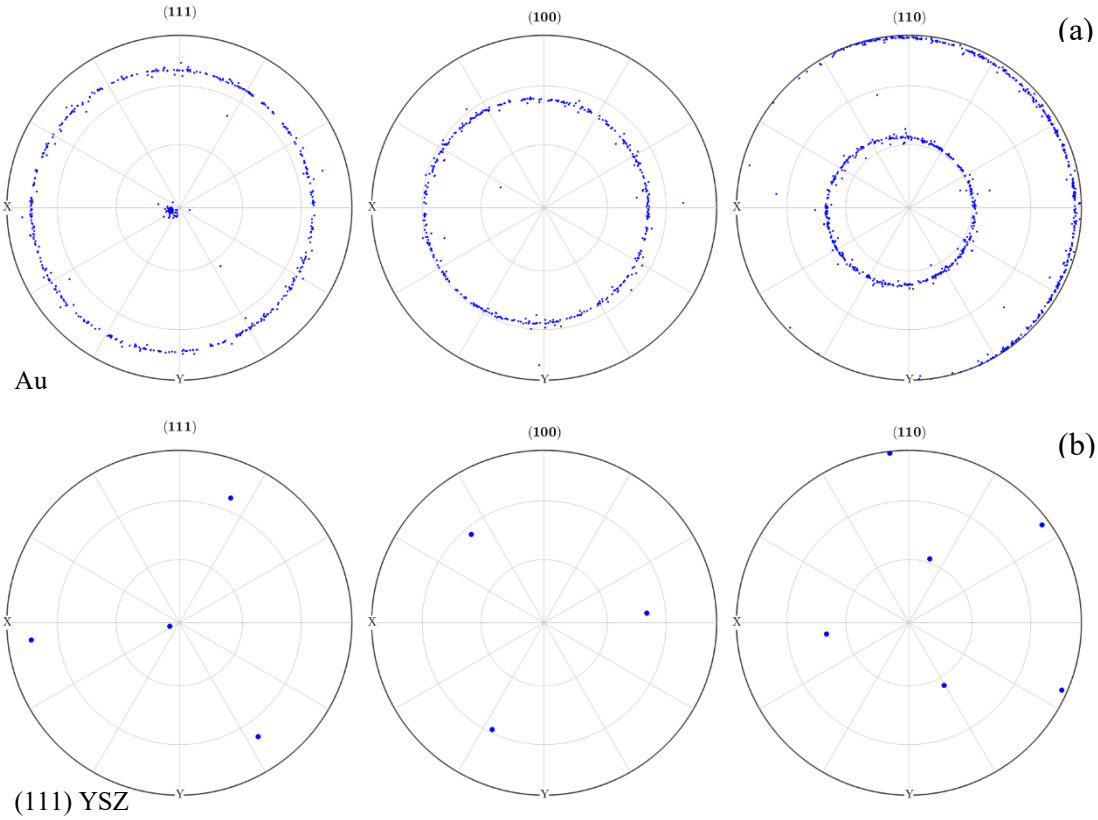

Figure 30: EBSD orientation relationship result of equilibrated Au particles (second dewetting experiment) and YSZ. (a) EBSD pole figures in 3 different pole directions of 150 equilibrated gold particles from the second solid state dewetting; (b) orientation of (111) YSZ substrate.

4.1.2.3 Interface Energy and Chemistry

Three Au particles with different in-plane orientations were prepared using FIB and characterized by TEM. Bright field micrographs and selected area diffraction patterns are shown in Figure 31. Two of the particles ((b) and (c)) are in a low-index orientation relationship with the substrate, which are $\mathrm{Au}\,[\bar{1}10](111) \parallel \mathrm{YSZ}\,[1\bar{1}0](111)$ and $\mathrm{Au}\,[1\bar{1}0](111) \parallel \mathrm{YSZ}\,[1\bar{1}0](111)$. Particle (a) is in a high-index orientation relationship that cannot be deciphered. In all three cases the interface was found to be flat and co-planar with the substrate surface.

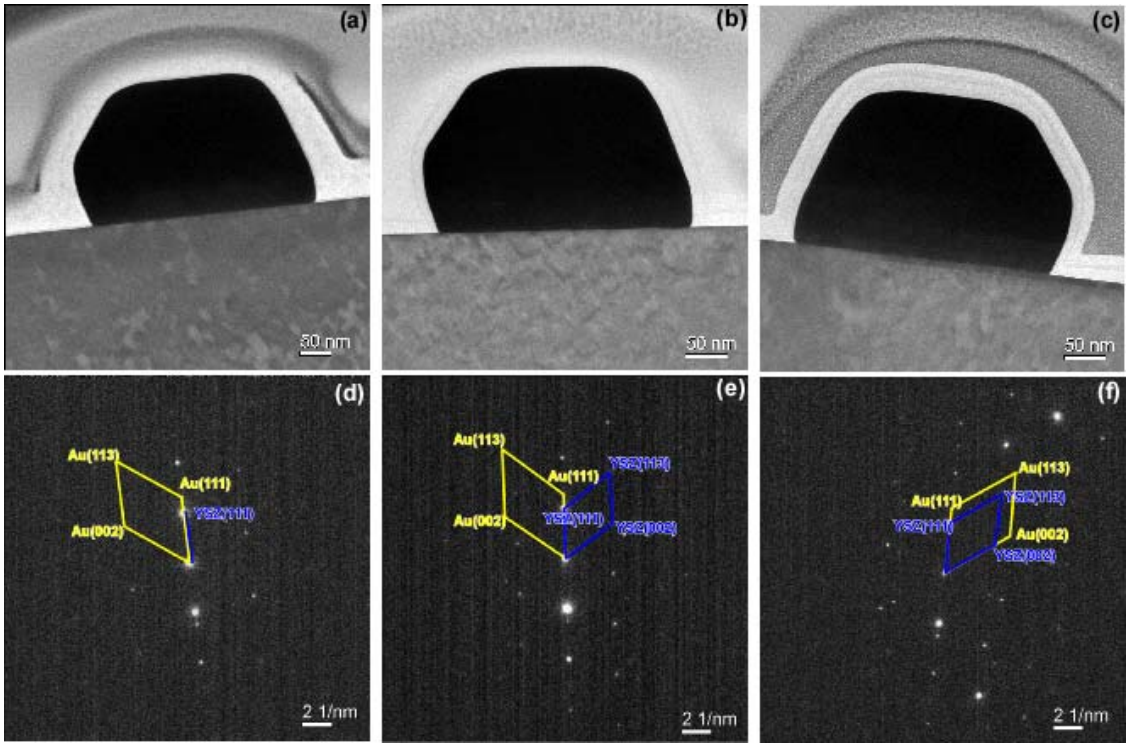

Figure 31: Bright field TEM micrographs of three equilibrated gold particles (black contrast) equilibrated on the YSZ substrate. (d), (e), and (f) are selected area diffraction patterns acquired from the interface region from (a), (b), and (c), respectively. All three particles were aligned in the $[\bar{1}10]$ zone axis before acquiring the micrographs and diffraction patterns.

Interface energy measurements were conducted on all the three equilibrated Au particles in Figure 31 using Winterbottom analysis. The results are shown in Table 5.

Table 7: Interface energy results from particle (a), (b), and (c) in Figure 31.

Particle	(a)	(b)	(c)
Interface energy(J/m^2)	1.61	1.59	1.61

The average interface energy from the three particles is **1.60 ± 0.01 J/m^2**.

Chemical characterization at the Au-YSZ interface from particle (c) in Figure 31 was conducted using HAADF STEM combined with EDS elemental mapping. In this case the YSZ substrate was aligned into a [110] zone axis so that the interface was parallel to the incident electron beam ("edge-on" conditions). Clear segregation of Cr and Y is shown in Figure 32, which confirmed by a quantitative line-scan of Cr and Y across the interface (Figure 33). Spatial difference spectrum were acquired from the interface region, and the Au and YSZ bulk (see Figure 34). A comparison of the Cr signal at the three areas with Figure 26 (b) further confirmed Cr excess at this interface.

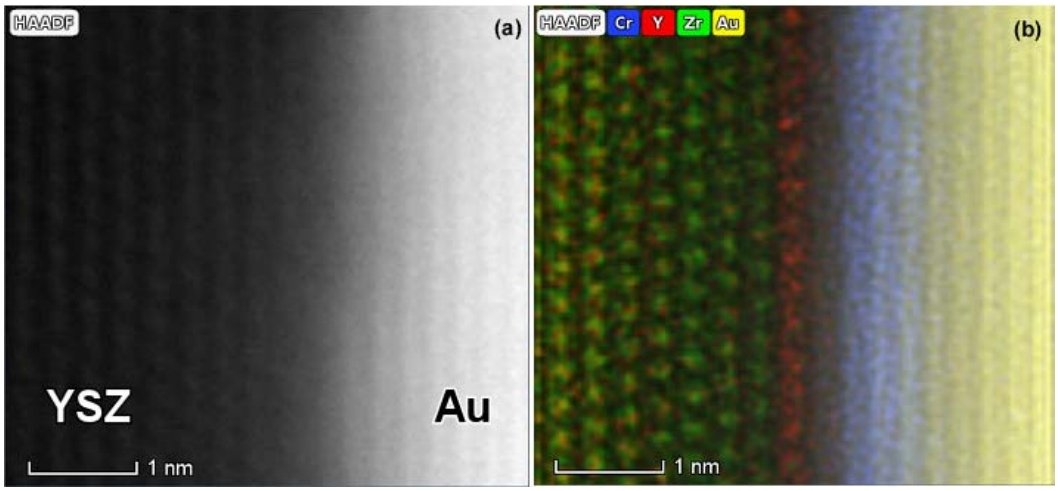

Figure 32: (a) HAADF STEM image of the interface of particle (a) in Figure 31. HAADF STEM image combined with EDS elemental mapping showing Cr segregation colored in blue at the interface, as well as Y segregation to the YSZ surface marked in red.

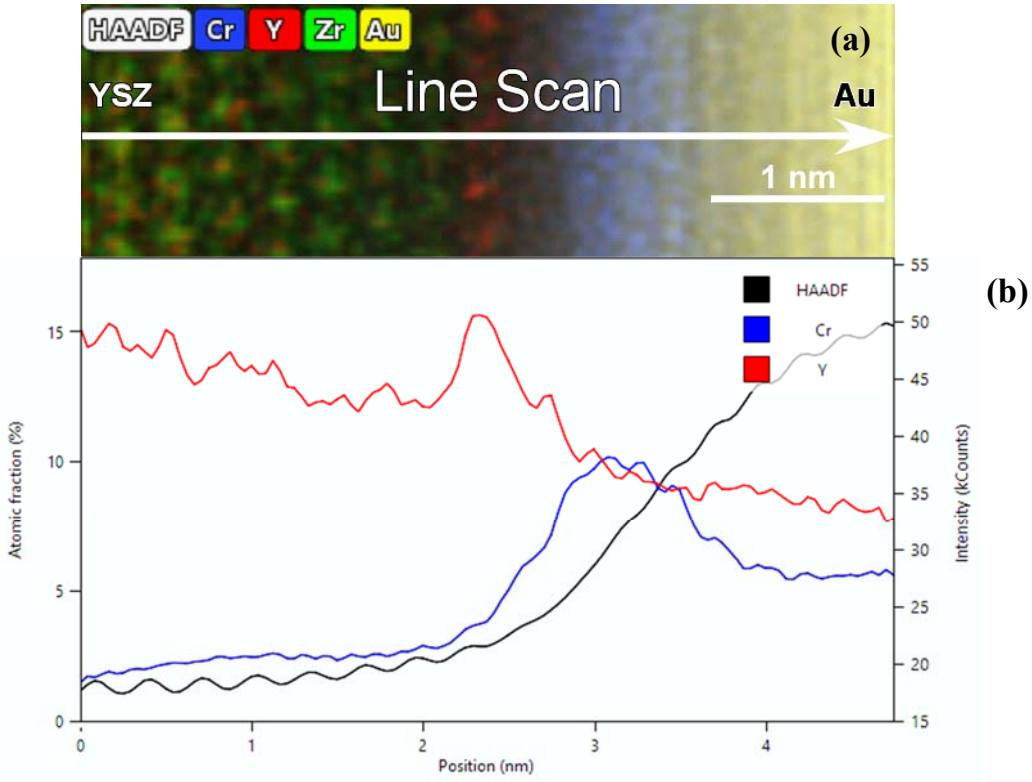

Figure 33:: (a) Arrow of line scan across the interface in STEM EDS elemental mapping. (b) Line scan spectrum showing Cr and Y quantification at each position of the line scan arrow across the interface.

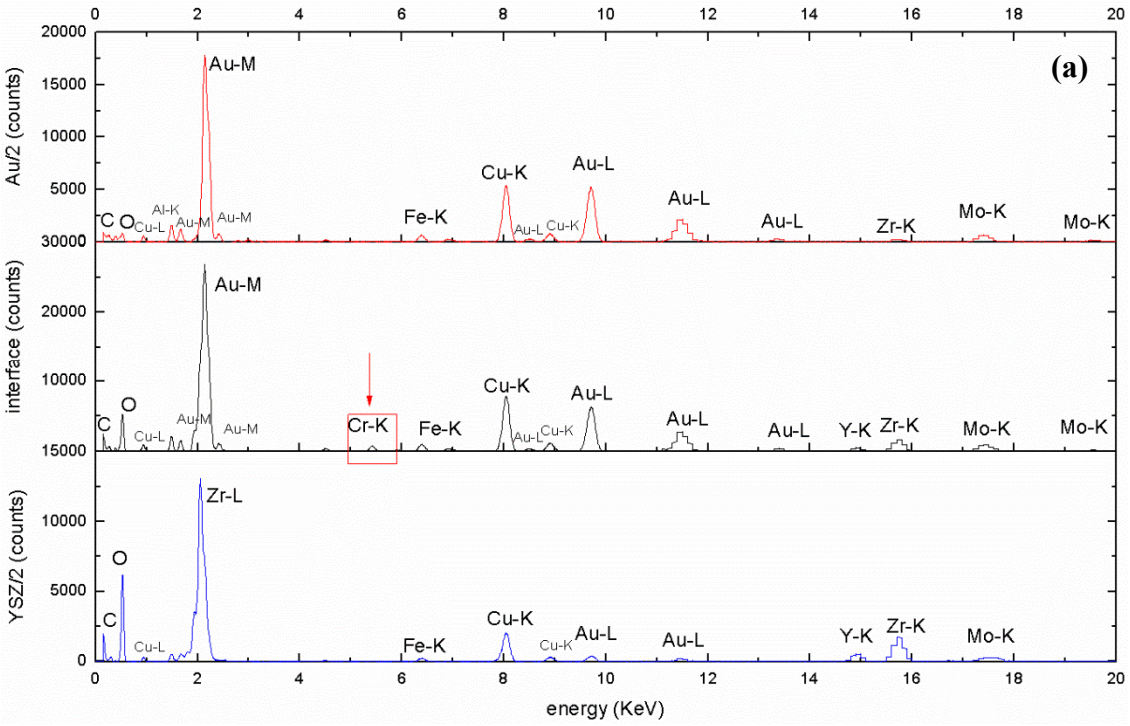

(b

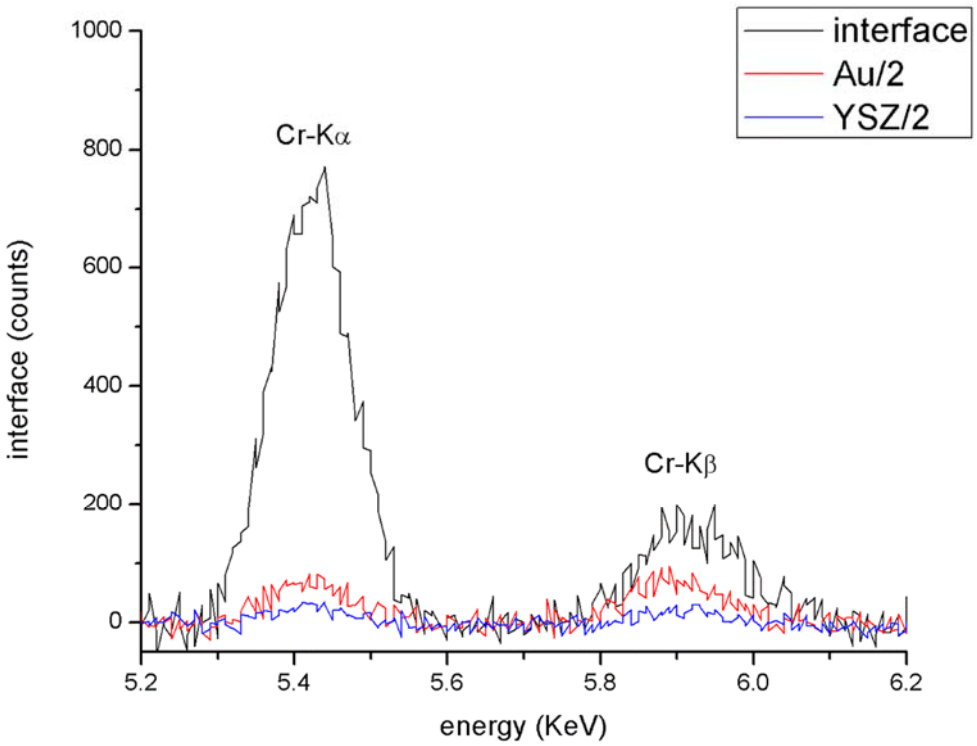

Figure 34: (a) EDS spatial difference result from the particle in Figure 31(c). The spectrum in red is the EDS signal from the bulk Au particle (away from the interface). The spectrum in black is the EDS signal from the interface region. The spectrum in blue is the EDS signal from the bulk YSZ (away from the interface). (b) Enlarged peak of Cr from the Au, interface and YSZ regions, showing Cr excess at the interface.

4.2 Solid and Liquid State Dewetting in Air

4.2.1 Dewetted Au Particle Morphology

4.2.1.1 Solid-State Dewetting

A representative plan-view SEM micrograph of a sample after solid-state dewetting in air is shown in Figure 35. Similar to solid-state dewetting of an e-beam evaporated sample in a controlled atmosphere, most of the particles are single crystalline, and only a small amount have grain boundaries. From the general morphologies of the dewetted particles, it is clear that not all of them are equilibrated, but all of them have an upper facet that is parallel to the substrate with a 3-fold symmetry in the sequence of the facets

at the side. This indicates that the particles in this experiment also have a strong preferred orientation of Au {111} ‖ YSZ {111}. Corroboration by XRD will be shown in the following text (Table 8).

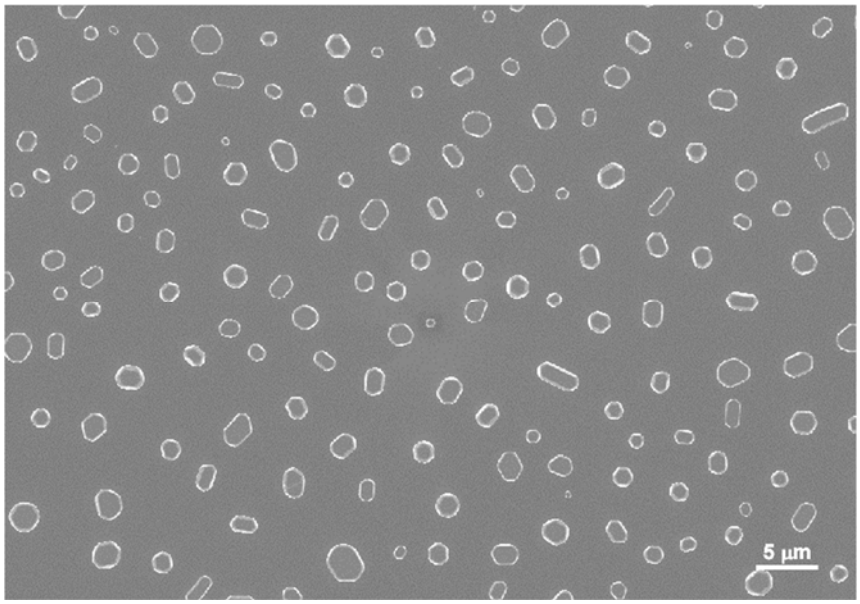

Figure 35: SEM plan-view micrograph of a sample after solid-state dewetting in air.

4.2.1.2 Liquid-State Dewetting

Unlike solid-state dewetting, where most of the particles are single crystalline, a significant number of particles from liquid-state dewetting showed polycrystalline or bi-crystalline morphology (see Figure 36).

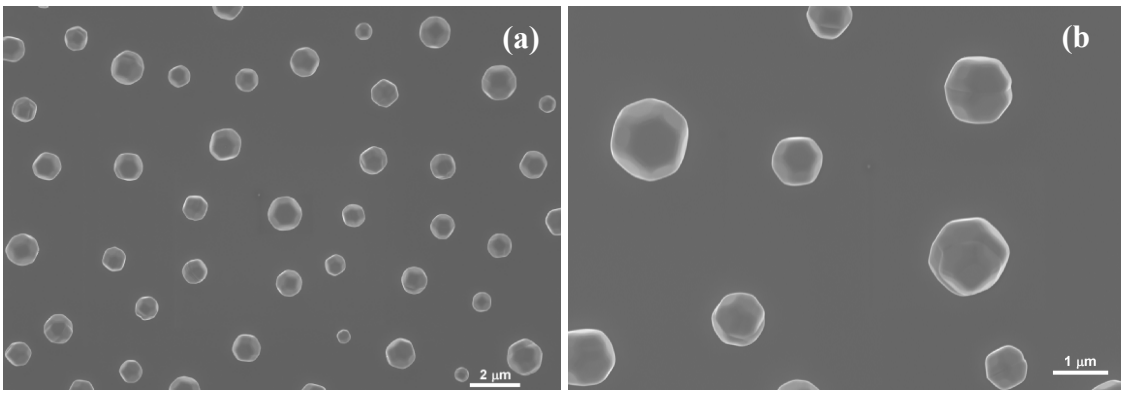

Figure 36: SEM micrographs of (a) Au particles on the YSZ surface after liquid-state dewetting in air. (b) is a higher magnification micrograph of single crystalline

and polycrystalline Au particles. The particles were equilibrated at 1000˚C for 48 hours after the liquid-state dewetting.

Representative morphologies of single crystalline Au particles after liquid-state dewetting are shown in Figure 37. Unlike the three-fold symmetry of single crystalline Au particles from solid-state dewetting, the particles here also show different two-fold symmetries, which means an orientation of the Au particles parallel to substrate surface which is different from the solid-state dewetted particles. Particles with grain boundaries or steps are shown in Figure 38.

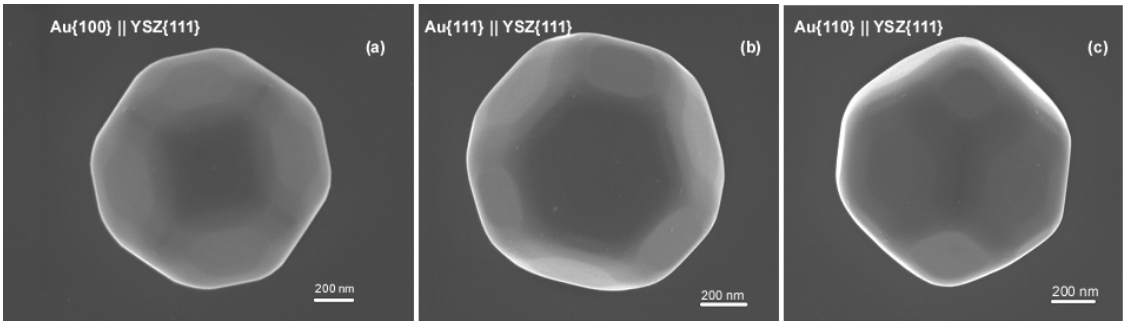

Figure 37: HRSEM micrographs showing the Au particle morphology with different preferred orientations, after liquid-state dewetting in air, followed by annealing at 1000˚C for 48 hours. (a) Particle showing an orientation of Au {100} || YSZ{111}; (b) Particle showing an orientation of Au{111} || YSZ{111}; (c) Particle showing an orientation of Au {110}||YSZ{111}

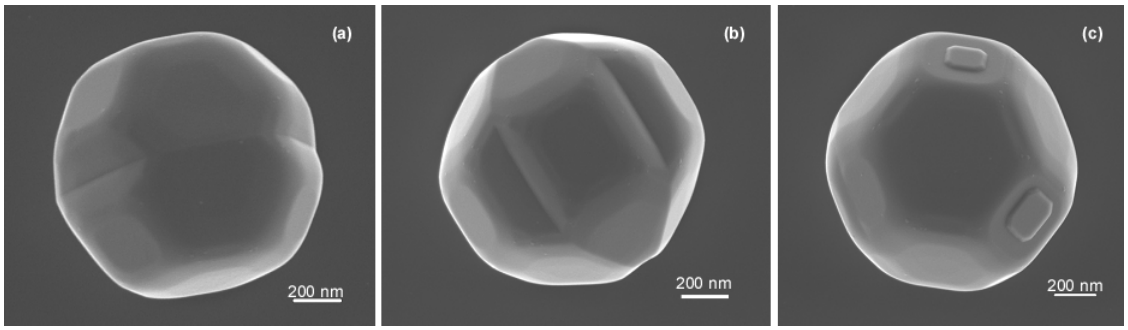

Figure 38: Morphology of Au particles with grain boundaries and steps. Particles were annealed at 1000˚C for 48 hours after liquid-state dewetting in air. (a) Bi-crystalline Au particle showing a twin; (b) Polycrystalline Au particle showing multiple twins; (c) A particle showing steps on {100} facet planes that outline the facet shape.

4.2.2 Preferred Orientation

To characterize the orientation of the Au particles parallel to the substrate surface, XRD was conducted on the samples dewetted in air; both the liquid and solid-state dewetted samples. An XRD pattern from a liquid-state dewetted sample is shown in Figure 39. Reflections from a variety of facet families are visible in the spectrum, indicating that the orientation parallel to substrate surface is anisotropic. A comparison of the P ratio between solid and liquid-state dewetting is presented in Table 8.

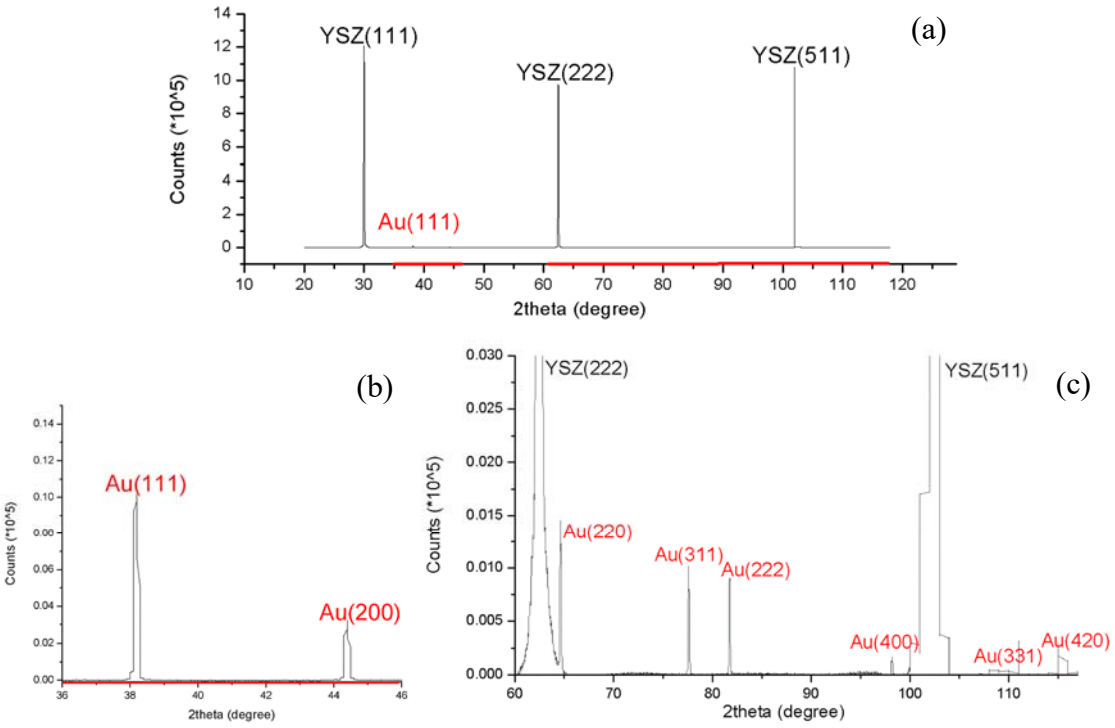

Figure 39: An XRD pattern from a sample after liquid-state dewetting. (a) is the full pattern acquired from 20° to 117°. (b) and (c) are segments of (a) and only include reflections from the gold particles.

Table 8: P ratio of the particles after liquid and solid-state dewetting.

Reflection (Au)	2θ	Standard intensity	P (**solid**-dewetted)	P (**liquid**-dewetted)
111	38.18	100	2.88	1.64
200	44.39	30.9	$5.5*10^{-3}$	0.98
220	64.58	13.8	--	0.71
311	77.55	10.5	0.001	0.48
331	110.8	6.5	0.0025	0.46
420	115.26	13.8	--	1.03

5. Discussion

5.1 Solid-State Dewetted Particle Morphology

5.1.1 Non-Equilibrated Morphology

The stability of non-equilibrated crystals from dewetting experiments was also noted and discussed in other works [17,35,81]. Shape evolution of a non-equilibrated form towards equilibration requires facet movements in a normal direction, where steps or defects on the faceted planes are required for facet motion (growth). However, for atomically flat facets without any pre-existing steps or defects, the nucleation energy barrier to form a step can be insurmountable [51,52]. Thus the stability of these large facets may be the reason for the immobile shape of the two categories of non-equilibrated shapes: the equi-axed shape with a large {111} facet plane parallel to the substrate surface as shown in Figure 16(b), and the elongated shape shown in Figure 16(a).

Malyi et al. suggested that the elongated single crystal could be a result of grain boundary motion to eradicate a bi-crystalline particle [81]. As mentioned in the results regarding the general morphology after solid-state dewetting, in this study most of the Au particles after solid-state dewetting are single crystalline. It was suggested in the model that for a bi-crystal with a certain misorientation, shape evolution towards a single crystal can be remarkably fast due to a high gradient of curvature. Sternlicht et al. characterized nanometer-length scaled steps (so called disconnections) at grain boundaries and correlated the step movement along the grain boundary as the mechanism for grain boundary motion [82]. This might explain the scarcity of grain boundaries found in the solid-state dewetted particles. Figure 40(a) shows a slightly curved elongated Au particle, resembling the final stage of grain rotation mechanism proposed by Malyi et al. (see Figure 41).

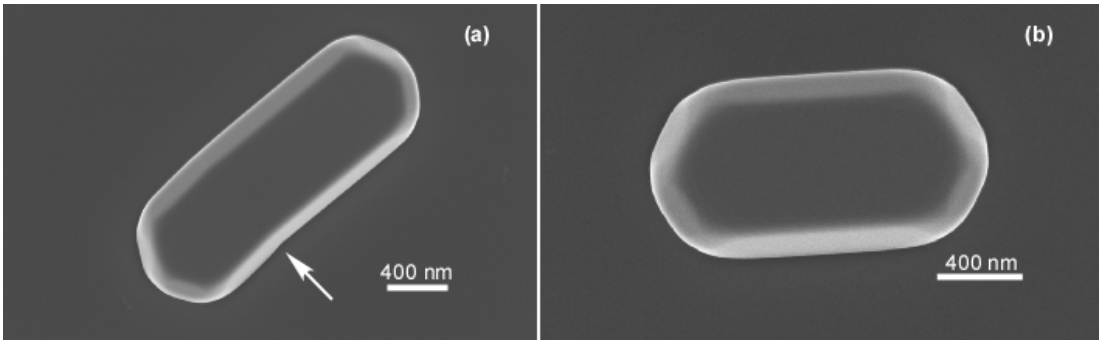

Figure 40: (a) Au particle found to be slightly curved (as indicated by the arrow); (b) Elongated Au particle.

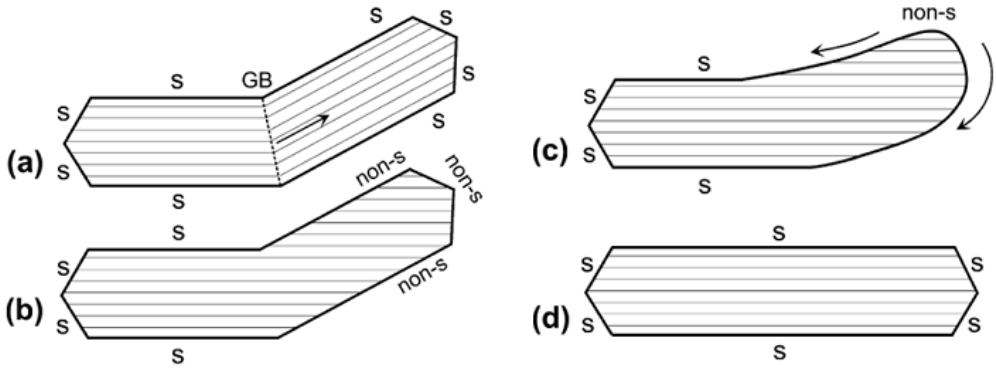

Figure 41: Illustration from [81]**. (a)-(b) Initial stage of bi-crystal shape evolution towards elongated single crystal.**

5.1.2 Equilibrated Morphology

The energy anisotropy between {111} and {100} facet planes obtained from the Au ECS in this study is $\gamma_{\{100\}}/\gamma_{\{111\}}=1.067$, which is close to $\gamma_{\{100\}}/\gamma_{\{111\}}=1.06$ found by Sadan et al. compared to other results in Table 1. But the equilibrium particle morphology from Sadan et al. seems to be more faceted (Figure 8(c)) compared to what was found in this work. It should be noted that their equilibration temperature was slightly higher (1000°C vs 950°C). The more faceted morphology implies deeper cusps at the {111} and {100} direction in the γ–plot compared to the other directions, which corresponds to the rounded surfaces. This could be a result of contamination species which segregate, changing the surface anisotropy at the surface because of different annealing atmospheres (air vs controlled PO_2). Increasing the surface energy anisotropy due to

segregation (or adsorption) was reported before for Ni and Bi doped Pb alloys [83], Bi-saturated Cu crystals [13], and oxygen adsorbed Cu crystals [84]. In this work, although the Ca excess was found at the interface, no visible excess was found at the (111) surface of Au according to the spatial difference technique (see Figure 26).

5.2 Interface Energy and Interface Structure

For the Au-(111) YSZ system, where the two phases have a similar cubic symmetry, the lock-in model suggests a cube-on-cube low energy configuration is expected to be preferred [23] . However, EBSD results showed that there is no low-index orientation relationship in this system, and the in-plane (interface plane) rotation of Au particles about the <111> direction is almost random (see Figure 42 (b, c)). For the Ni-(111) YSZ studied by Nahor, equilibrated interfaces formed using the same solid-state dewetting method were found to have two low-index orientation relationships [35]. One is $\mathrm{Ni}\,[1\bar{1}0](111) \parallel \mathrm{YSZ}[1\bar{1}0](111)$, i.e. the expected cube-on-cube configuration. The other is $\mathrm{Ni}\,[\bar{1}10](111) \parallel \mathrm{YSZ}[1\bar{1}0](111)$, where the Ni has a twinned orientation with the cubic substrate. These two orientations are rotated 180° to each other about the <111>

direction of the Ni (see Figure 42 (a)).

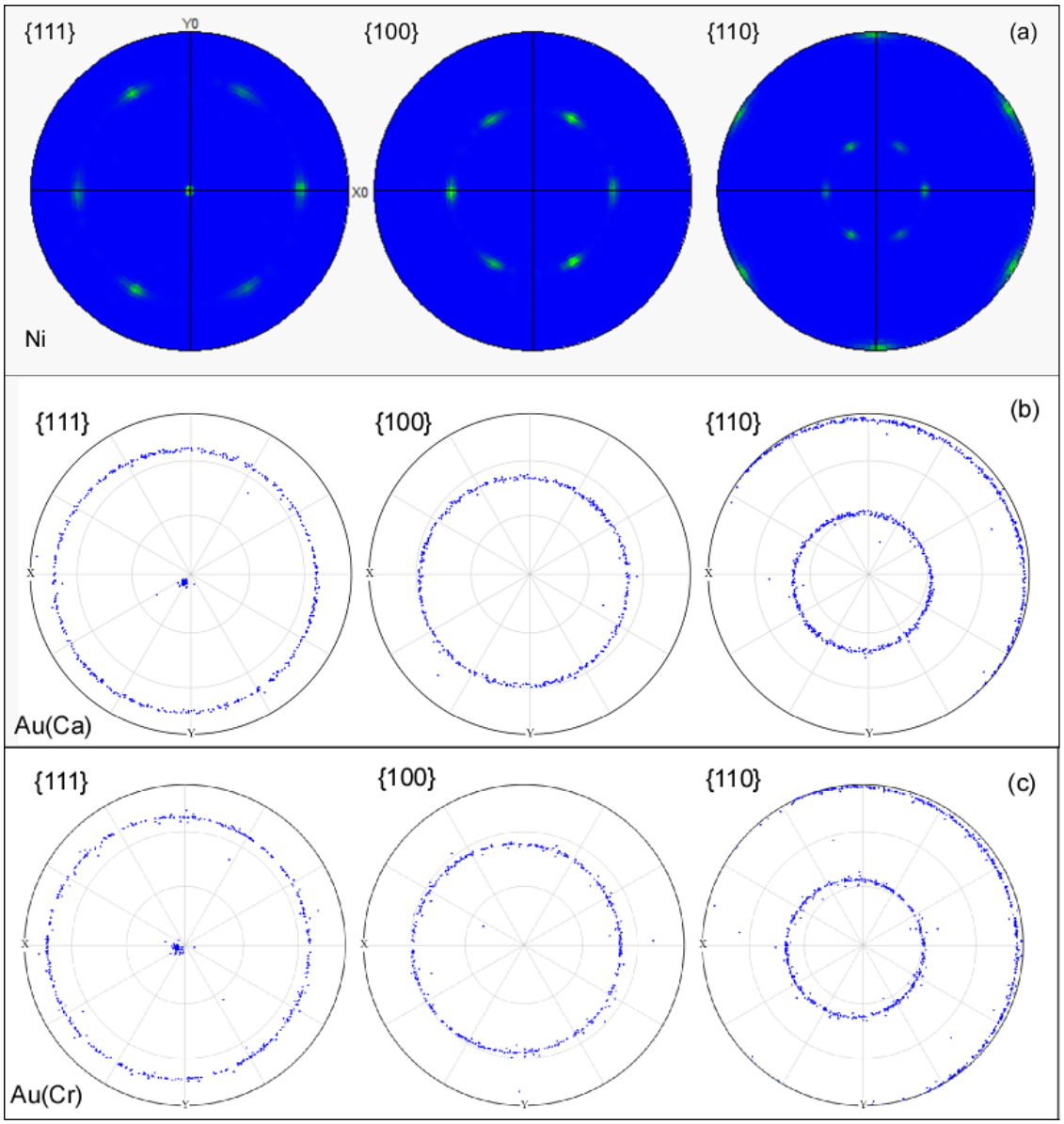

Figure 42: EBSD results showing orientation of equilibrated Ni and Au particles on (111) YSZ substrates. (a) for Ni from [35]**; (b) from Au/(111)YSZ with Ca segregation; (c) from Au/(111)YSZ with Cr segregation.**

Moreover, from EBSD of the Ni-(111) YSZ system, the intensity of the cube-on-cube orientation is slightly preferred compared to that of the twined orientation. This means the number of equilibrated particles with a cube-on-cube orientation is larger than the twined orientation. Interface energy measurements from the Ni system also revealed a lower interface energy for the cube-on-cube orientation (1.8 ± 0.1 J/m^2) than the twined orientation (2.0 ± 0.1 J/m^2). This is presumably the reason for the preference between the two orientations.

For the Au-(111) YSZ system, the interface energy of three particles in the Ca segregated samples were measured to be 1.75 ± 0.02 J/m^2. For the three from the Cr segregated samples, the interface energy was determined to be 1.60 ± 0.01 J/m^2. This means the interface energies for the different (high-index) orientation relationships in each system (Ca vs. Cr doped) are almost identical given the standard deviations. This explains the random rotation of Au particles on YSZ as a result of no orientation relationship, since all configurations are almost identical in their interface energies.

The Au-(111) YSZ interface energies in this study were determined either in the presence of Ca or Cr segregation. Assuming the surface energy of (111) Au (1.4 J/m^2[5]) and (111) YSZ (1.17 J/m^2[85]) remain the same (no segregation to these surfaces), the interface energies are 1.75 ± 0.02 J/m^2 and 1.60 ± 0.01 J/m^2 for Ca and Cr, respectively. However, following the concept of segregation according to Gibbs, these values must be lower than the clean Au-(111) YSZ interface (without segregation) [86]. The fact that the interface energy with Cr segregation is lower and that of the interface with Ca segregation could be due to different amounts of segregants, and/or the difference in chemical bonding of the two segregating species.

5.3 Interface Chemistry and Interface Structure

The equilibrated Au-(111) YSZ interfaces studied in this work were found to have no preferred in-plane orientation relationship, but to have either Ca or Cr segregation at the interface. An important question is whether or not the segregation changed the interface structure. Nahor et al. studied interface orientation of both Cr segregated and Cr-Fe co-segregated Ni/(111)YSZ interfaces, and found no influence of the segregating species on the orientation relationship (although the ECS of Ni was changed) [35]. In comparison, in the case of Au-(0001) sapphire, Baram et al. found that Ca and Si co-segregation at the interface decreased the in-plane anisotropy compared to the case of un-doped Au-(0001) sapphire where Sadan et al. found two low index orientation relationships [66,87]. The two cases above are used to discuss the segregation effect related to the macroscopic degrees of freedom (the orientation relationship). Details on the atomistic structure are not known and thus not included in the discussion. In the present work, whether Ca or Cr segregation reduced the anisotropy of the pure macroscopic degrees of freedom is not known.

From a microscopic point of view, Kaplan et al. studied Ca segregation in the Al-(0001) α-Al_2O_3 interface [88]. In their study, four cation layers of Ca were found at the interface. The symmetry and periodicity of the interface were found to be of significantly different from that of bulk α-Al_2O_3 and bulk Al. This means reconstruction at the interface happened due to Ca segregation. In a similar manner, Gautier et al. found 2×2 reconstructed α-Al_2O_3 surface after Ca segregation [89]. In other examples, Cr was used in various metal-ceramic systems to improve adhesion, presumably by segregation [90–92]. Segregation of Cr to the interface can result in a rearrangement of atoms to a more low-energy configuration, resulting in a higher work of adhesion [93]. Thus, it is obvious that interfacial segregation can change the microscopic structure at the interface, and it has been shown to change a low-index orientation relationship to a simple preferred orientation for Ca-Si doped Au-(0001) sapphire interfaces, but whether this occurs in the present system is not yet clear.

5.4 The Difference between Solid and Liquid State Dewetting

5.4.1 Interface Preferred Orientation

Solid state dewetting: From the XRD results, a strong peak of (111) Au from as-deposited sample indicates the preferred orientation Au(111) ∥ YSZ(111) exists after deposition and before dewetting. This was also found in Ni-(111)YSZ and (001)YSZ[35], Pt-(111)YSZ and (001)YSZ[94], Au-(0001) sapphire [95,96]. Thin films deposited on foreign substrates have a large surface area compared to their thickness. To reduce the total energy of the system, a polycrystalline film might prefer to adopt a texture of a (111) oriented free surface which has the lowest surface energy for most FCC metals, and the close-packed structure of (111) in contact with the substrate might improve bonding at the interface and result in a lower interface energy. After solid-state dewetting this orientation is retained and even further strengthened (increase in the XRD intensity of (111) Au, see Figure 19, Figure 20, Figure 28, and Figure 29). According to Beck et al., an as-deposited Pt nano-crystalline film has a high concentration of stacking faults and twins whose removal after solid-state dewetting was found to be associated with the increase in intensity and decrease in broadness of the preferred reflection [94].

Liquid state dewetting: In liquid-state dewetting, the kinetic process of dewetting will be faster than in the solid-state. After rupture, during cooling to the solid-state temperature used for annealing, nucleation will occur. If during this process, nucleation randomly occurs inside the liquid drop (homogeneous nucleation), a random orientation of the Au particles should be found. However, since the Au film is in contact with the (111) YSZ substrate, heterogeneous nucleation is more likely to occur, forming Au precipitates oriented with the substrate. As a result, a preferred orientation above the random frequency (P>1, see Equation (18)) should be found. For the Au-YSZ system after liquid-state dewetting, a preferred orientation of Au (111) ∥ YSZ (111) above the random frequency was found from XRD. For the other orientations parallel to the substrate, which are (200), (220), (311), (331) and (420), only two are at the level of random frequency, (200) and (420). The others are below random. The discrepancies of other orientations below random could be a systematic error from the measurement or these orientations are just thermodynamically un-preferred. Compared to the single Au (111) ∥ YSZ (111) in solid-state dewetting, the preferred orientation of the liquid is the same but with more diversity in the other orientations that are close to or below the random frequency. This could be due to the nucleation process. Differences in orientation due to liquid versus solid-state dewetting was investigated by Curiotto et al. for Cu on (0001) sapphire [24]. An orientation above a random frequency of Cu (111), (110), (311) and (210) parallel to (0001) sapphire was found in liquid-state dewetting, while only a single orientation of Cu (111) ∥ Al_2O_3 (0001) was found in solid-state dewetting. AFM results from the surface morphology show that step edges running along the $<2\bar{1}\bar{1}0>$ direction exist on the (0001) surface of Al_2O_3. Orientation results from liquid dewetting showed that except for the $Cu[\bar{1}10]||Al_2O_3[10\bar{1}0]$ that was found after solid-state dewetting, $Cu[\bar{1}10]||Al_2O_3[2\bar{1}\bar{1}0]$ also exists. The additional orientation found in liquid-state dewetting was due to nucleation at the step edges that are oriented along the $<2\bar{1}\bar{1}0>$ direction. Under this configuration, if the energy difference between the (111), (110), (311) and (210) parallel to the (0001) surface of sapphire is small, all of these configurations will be preferred and found to be above random frequency.

5.4.2 Grain Boundaries and Liquid State Dewetting

The high frequency of appearance of polycrystalline particles was also reported for liquid-state dewetting of Cu and Au on c-sapphire [12,24,66]. Many of the grain boundaries from the work of Sadan et al. (Au/c-sapphire) and Curiotto et al. (Cu/c-sapphire), were found to be twin boundaries [24,66]. In this work, high angle grain boundaries were also found, and many of the grain boundaries were found to be in a mirror symmetry at the two sides of the boundary(see Figure 38 (a), (b)), which indicates that these boundaries are twin boundaries. Annealing twins can form due to mechanical deformation or annealing processes, or as in this study during the solidification of the liquid dewetted Au droplets. Several models were proposed to understand the twinning formation mechanism [97–100], where most of the models were developed based on the growth accident theory proposed by Carpenter et al. [101]. Twin boundaries, especially coherent twin boundaries, are associated with a much lower grain boundary energy compared to other high angle grain boundaries. As a result twin boundaries are more stable and appear with a higher frequency.

6. Summary and Conclusions

The main goal of this study was to determine the interface energy and orientation relationship between undoped Au-YSZ interfaces, and the influence of segregation on these properties, as well as the equilibrium crystal shape of Au. To obtain both Au-YSZ interfaces and the Au ECS, Au thin films deposited on the (111) surface of YSZ single crystalline substrates were dewetted and equilibrated. Two different substrate cleaning processes were used in an attempt to prepare clean Au-YSZ interfaces by solid-state dewetting. Interfaces from the first and second solid-state dewetting were found to have Ca and Cr segregation, respectively. EBSD results of 150 equilibrated Au particles from both experiments showed that there is no preferred low-index orientation relationship (or in-plane orientation relationship) between Au and YSZ. This result was associated with identical interface energies measured from equilibrated Au particles with different orientation relationships with the YSZ substrate. The orientation of Au parallel to the YSZ substrate in both experiments was also analyzed using XRD, and no significant change was found in the preferred orientation of {111} Au|| {111} YSZ before and after solid-state dewetting.

Interface energies measured from both experiments were found to be 1.75 ± 0.02 J/m^2 and 1.60 ± 0.01 J/m^2 for Ca and Cr segregated systems, respectively, assuming no change in the (111) surface energy of Au or the YSZ substrate. The difference in the interface energy may due to different quantities and/or chemistry of Ca and Cr segregants. No un-doped Au-YSZ interface was obtained. Comparisons to other systems were made, but no conclusions can be drawn regarding whether or not Ca and Cr change the interface structure.

For comparison, both liquid-state and solid-state dewetting were conducted in air to produce Au particles. Many of the liquid-dewetted particles were found to be poly-crystalline particles with grain boundaries, while in solid-state dewetting most of the particles were single crystals. Liquid-state dewetting was also found to increase the isotropy of orientation of Au parallel to the YSZ substrate, perhaps due to the nucleation process.

7. Suggestions for Future Work

Clean Au-YSZ substrate need to be prepared and characterized in order to determine whether segregation can change the atomistic structure of the interface.

The metal-ceramic chemistry need to be explored to understand why random orientation relationships exist between Au-YSZ, while a low-index orientation relationship is preferred for Ni-YSZ (even with Cr segregation).

Different amounts of Ca or Cr dopant should be added into the Au-YSZ system to study the influence of different solute activity on segregation and excess interface energy.

The in-plane orientation relationship of liquid dewetted Au-YSZ need to be determined by EBSD to see if there is also a random distribution of orientation relationships, like for solid-state dewetted Au particles.

More interface energy measurements of equilibrated particles having various orientations parallel to the substrate from liquid-state dewetting experiment should be conducted.

In-situ heating experiment in TEM might be one way to observe the nucleation process of liquid Au in contact with YSZ.

The ECS of Au from dewetting experiments in air and controlled atmosphere should be compared to determine whether the annealing atmosphere influences the ECS.

Chemical analysis of surface facets on the ECS of Au equilibrated from solid-state dewetting experiments need to be done to see whether adsorption exists on the particle surface.

8. References

[1] Zhang W B, Chen C and Zhang S Y 2013 Equilibrium crystal shape of Ni from first principles *J. Phys. Chem. C* **117** 21274–80

[2] Galanakis I, Papanikolaou N and Dederichs P H 2002 Applicability of the broken-bond rule to the surface energy of the fcc metals *Surf. Sci.* **511** 1–12

[3] Rajagopal A K and Callaway J 1973 Inhomogeneous electron gas *Phys. Rev. B* **7** 1912–9

[4] Lejček P, Šob M and Paidar V 2017 Interfacial segregation and grain boundary embrittlement: An overview and critical assessment of experimental data and calculated results *Prog. Mater. Sci.* **87** 83–139

[5] Kumikov V K and Khokonov K B 1983 On the measurement of surface free energy and surface tension of solid metals *J. Appl. Phys.* **54** 1346–50

[6] Tyson W R and Miller W A 1976 Surface free Energies of Solid Metals-Estimation from Liquid Surface Tension Measurements *Surf. Sci. Rep.* **62** 267–76

[7] de Boer F R, Boom R, Mattens W C M, Miedema A R and Niessen A K 1989 Cohesion in Metals: Transition Metal Alloys *Cohes. Struct.*

[8] G. Wulff 1901 Zur frage der geschwindigkeit des wachstums und der auflosung der krystalflachen *Z. Kryst. Miner.* **34** 449–530

[9] Ringe E, Van Duyne R P and Marks L D 2011 Wulff construction for alloy nanoparticles *Nano Lett.* **11** 3399–403

[10] Laue M v. 1943 Der Wulffsche Satz für die Gleidigewichtsform von Kristallen *Zeitschrift für Krist. - Cryst. Mater.* **105** 124– 133

[11] Dinghas A 1944 Uber einen geometrischen sat von Wulff fur die gleichgewitchtsform von kristallen *Z. Krist.* **105** 304–14

[12] Chatain D, Ghetta V and Wynblatt P 2004 Equilibrium Shape of Copper Crystals Grown on Sapphire *Interface Sci.* **12** 7–18

[13] Chatain D, Wynblatt P and Rohrer G S 2005 Equilibrium crystal shape of Bi-saturated Cu crystals at 1223 K *Acta Mater.* **53** 4057–64

[14] Lapujoulade J 1994 The roughening of metal surfaces *Surf. Sci. Rep.* **20** 195–249

[15] Wynblatt P and Chatain D 2009 Surface segregation anisotropy and the equilibrium shape of alloy crystals *Rev. Adv. Mater. Sci.* **21** 44–56

[16] Chatain D 2008 Anisotropy of Wetting *Annu. Rev. Mater. Res.* **38** 45–70

[17] Meltzman H, Chatain D, Avizemer D, Besmann T M and Kaplan W D 2011 The equilibrium crystal shape of nickel *Acta Mater.* **59** 3473–83

[18] N.E. Dorsey 1928 No Title *J. Washingt. Acad. Sci.* **18** 505

[19] Saiz E, Tomsia A P and Cannon R M 1998 Ridging effects on wetting and spreading of liquids on solids *Acta Mater.* **46** 2349–61

[20] Saiz E, Cannon R M and Tomsia A P 2000 Enhanced atomic transport at liquid metal/Al2O3 interfaces *Adv. Mater.* **12** 1952–5

[21] Levi G and Kaplan W D 2002 Oxygen induced interfacial phenomena during wetting of alumina by liquid aluminium *Acta Mater.* **50** 75–88

[22] Taylor P, Lejček P, Hofmann S and Lejtekl P 2013 Critical Reviews in Solid State and Materials Sciences Thermodynamics and structural aspects of grain boundary segregation Thermodynamics and Structural Aspects of Grain Boundary Segregation **20(1)** 37–41

[23] Fecht H J and Gleiter H 1985 A lock-in model for the atomic structure of interphase boundaries between metals and ionic crystals *Acta Metall.* **33** 557–62

[24] Curiotto S, Chien H, Meltzman H, Wynblatt P, Rohrer G S, Kaplan W D and Chatain D 2011 Orientation relationships of copper crystals on c-plane sapphire *Acta Mater.* **59** 5320–31

[25] James M. Howe 1997 *Interfaces in Materials: atomic structure, thermodynamics and kinetics of solid-vapor, solid-liquid and solid-solid interfaces* (John Wiley & sons, Inc)

[26] Nahor H and Kaplan W D 2016 Structure of the Equilibrated Ni(111)-YSZ(111) Solid-Solid Interface *J. Am. Ceram. Soc.* **99** 1064–70

[27] Meltzman H, Mordehai D and Kaplan W D 2012 Solid-solid interface reconstruction at equilibrated Ni-Al2O3interfaces *Acta Mater.* **60** 4359–69

[28] Liu F, Xie D Y, Bugnet M, Majdi T, Preston J S, Wang J and Zhu G zhen 2018 Temperature-Induced Atomic Reconstruction At Au/MgAl2O4Interfaces *Adv. Mater. Interfaces* **1701664** 2–7

[29] Finnis M W 1999 The theory of metal - ceramic interfaces *J. Phys. Condens. Matter* **8** 5811–36

[30] Koberidze M, Puska M J and Nieminen R M 2018 Structural details of Al/Al2O3 junctions and their role in the formation of electron tunnel barriers *Phys. Rev. B* **97** 1–11

[31] Yadav S K, Shao S, Wang J and Liu X Y 2015 Structural modifications due to interface chemistry at metal-nitride interfaces *Sci. Rep.* **5** 1–9

[32] Winterbottom W L 1967 Equilibrium shape of a small particle in contact with a foreign substrate *Acta Metall.* **15** 303–10

[33] Pilliar R M and Nutting J 1967 Solid-solid interfacial energy determinations in metal ceramic systems *Philos. Mag.*

[34] Cahn J l. and Hoffman D l. 1974 A vector thermodlnamics for anisotropic surfaces-II. Curved and faceted surfaces *Acta Metall.*

[35] Nahor H (Bratt) 2018 *Structure and Thermodynamics of Solid-Solid Ni-YSZ Interfaces* (Technion-Israel Institute of Technology)

[36] Wynblatt P and Chatain D 2006 Anisotropy of segregation at grain boundaries and surfaces *Metall. Mater. Trans. A Phys. Metall. Mater. Sci.* **37** 2595–620

[37] Wynblatt P and Chatain D 2006 Anisotropy of segregation at grain boundaries and surfaces *Metall. Mater. Trans. A Phys. Metall. Mater. Sci.*

[38] Altomare M, Nguyen N T and Schmuki P 2016 Templated dewetting: designing entirely self-organized platforms for photocatalysis *Chem. Sci.* **7** 6865–86

[39] Guan Y F, Pearce R C, Melechko A V., Hensley D K, Simpson M L and Rack P D 2008 Pulsed laser dewetting of nickel catalyst for carbon nanofiber growth *Nanotechnology* **19**

[40] Mizsei J 1993 Activating technology of SnO2 layers by metal particles from ultrathin metal films *Sensors Actuators B. Chem.* **16** 328–33

[41] Robertson J 2004 High density plasma enhanced chemical vapor deposition of optical thin films *Eur. Phys. J. Appl. Phys.* **28** 265–91

[42] Nichols F A and Mullins W W 1965 Surface-(Interface-) and volume diffusion contributions to morphological changes driven by capillarity *Metall. Soc. Am. Inst. Mining, Metall. Pet. Eng. -- Trans.* **233** 1840–8

[43] Mullins W W 1959 Flattening of a nearly plane solid surface due to capillarity *J. Appl. Phys.* **30** 77–83

[44] D. J. Srolovitz and S. A. Safran 1986 Capillary instabilities in thin films *J. Appl. Phys.* **60** 1153–60

[45] Thompson C V. 2012 Solid-State Dewetting of Thin Films *Annu. Rev. Mater. Res.* **42** 399–434

[46] Génin F Y, Mullins W W and Wynblatt P 1992 Capillary instabilities in thin films: A model of thermal pitting at grain boundary vertices *Acta Metall. Mater.* **40** 3239–48

[47] Génin F Y, Mullins W W and Wynblatt P 1994 Capillary instabilities in polycrystalline metallic foils: Experimental observations of thermal pitting in nickel *Acta Metall. Mater.* **42** 1489–92

[48] Kaplan W D, Chatain D, Wynblatt P and Carter W C 2013 A review of wetting versus adsorption, complexions, and related phenomena: The rosetta stone of wetting *J. Mater. Sci.* **48** 5681–717

[49] Nichols F A and Mullins W W 1965 Surface- (interface-) and volume-diffusion contribution to morphological changes driven by capillarity *Trans. Met. Soc. AIME* **233** 1840–8

[50] Burton K 1949 CRYSTAL GROWTH AND SURFACE STRUCTURE Part I BY 33–9

[51] Rohrer G S, Rohrer C L and Mullins W W 2001 Nucleation energy barriers for volume-conserving shape changes of crystals with nonequilibrium morphologies *J. Am. Ceram. Soc.* **84** 2099–104

[52] Mullins W W and Rohrer G S 2000 Nucleation barrier for volume-conserving shape changes of faceted crystals *J. Am. Ceram. Soc.* **83** 214–6

[53] E. C. Subbarao 1980 *Solid Electrolytes and Their Applications* (NEW YORK AND LONDON)

[54] Tsunoda T, Hayakawa T, Imai Y, Kameyama T, Takehira K and Fukuda K 1995 Propene oxidation over MoO3 film deposited on an Au|YSZ|Ag system *Catal. Today* **25** 371–6

[55] Hamakawa S, Sato K, Hayakawa T, York A P E, Tsunoda T, Suzuki K, Shimizu M and Takehira K 1997 Selective oxidation of ethane using the Au vertical bar YSZ vertical bar Ag electrochemical membrane system *J. Electrochem. Soc.* **144** 1–5

[56] Sirinakis G, Siddique R, Manning I, Rogers P H and Carpenter M A 2006 Development and characterization of Au-YSZ surface plasmon resonance based sensing materials: High temperature detection of CO *J. Phys. Chem. B* **110** 13508–11

[57] Grunwaldt J-D, Maciejewski M, Becker O S, Fabrizioli P and Baiker A 1999 Comparative Study of Au/TiO2 and Au/ZrO2 Catalysts for Low-Temperature CO Oxidation *J. Catal.* **186** 458–69

[58] Zhang X, Wang H and Xu B Q 2005 Remarkable nanosize effect of zirconia in Au/ZrO2catalyst for CO oxidation *J. Phys. Chem. B* **109** 9678–83

[59] Rogers P H, Sirinakis G and Carpenter M A 2008 Direct observations of electrochemical reactions within Au-YSZ thin films via absorption shifts in the Au nanoparticle surface plasmon resonance *J. Phys. Chem. C* **112** 6749–57

[60] Takeguchi T, Kikuchi R, Yano T, Eguchi K and Murata K 2003 Effect of precious metal addition to Ni-YSZ cermet on reforming of CH4and electrochemical activity as SOFC anode *Catal. Today* **84** 217–22

[61] Haruta M 2002 Catalysis of gold nanoparticles deposited on metal oxides *CATTECH*

[62] Wang Z and Wynblatt P 1998 The equilibrium form of pure gold crystals *Surf. Sci.* **398** 259–66

[63] JC H and JJ M 1980 Shape of Gold Graphite Cleavage on a Surface Energies *Acta mettalurgica* **28** 1789

[64] Sivaramakrishnan S, Wen J, Scarpelli M E, Pierce B J and Zuo J M 2010 Equilibrium shapes and triple line energy of epitaxial gold nanocrystals supported on TiO2(110) *Phys. Rev. B - Condens. Matter Mater. Phys.*

[65] Wang Z and Wynblatt P 1998 Wetting and energetics of solid Au and Au-Ge/SiC interfaces *Acta Mater.* **46** 4853–9

[66] Sadan H and Kaplan W D 2006 Au-Sapphire (0001) solid-solid interfacial energy *J. Mater. Sci.* **41** 5099–107

[67] Gangopadhyay U and Wynblatt P 1995 Modification of the gold/graphite interfacial energy by interfacial adsorption of nickel *J. Mater. Sci.* **30** 94–100

[68] Sadan H 2006 *Energy and Morphology of Solid-Solid Au-Sapphire Interfaces*

[69] Li P, Chen I W and Penner-Hahn J E 1993 X-ray-absorption studies of zirconia polymorphs. II. Effect of Y2O3 dopant on ZrO2 structure *Phys. Rev. B*

[70] Catlow C R A, Chadwick A V, Greaves G N and Moroney L M 1986 EXAFS Study of Yttria-Stabilized Zirconia *J. Am. Ceram. SOC*

[71] Scott H G 1975 Phase relationships in the zirconia-yttria system *J. Mater. Sci.*

[72] Baram M and Kaplan W D 2008 Quantitative HRTEM analysis of FIB prepared specimens *J. Microsc.* **232** 395–405

[73] Reyntjens S and Puers R 2001 A review of focused ion beam applications in microsystems technology *J. Micromechanics Microengineering* **11** 287–300

[74] Sivel V G M, Van Den Brand J, Wang W R, Mohdadi H, Tichelaar F D, Alkemade P F A and Zandbergen H W 2004 Application of the dual-beam FIB/SEM to metals research *J. Microsc.* **214** 237–45

[75] Zucker R V., Chatain D, Dahmen U, Hagege S and Carter W C 2012 New software tools for the calculation and display of isolated and attached interfacial-energy minimizing particle shapes *J. Mater. Sci.* **47** 8290–302

[76] Anon 2013 International Center for Diffraction Data(Y0.15Zr0.85O1.93-00-030-1468)

[77] Anon International Center for Diffraction Data(Au-00-004-0784)

[78] Keast V J and Williams D B 2000 Quantification of boundary segregation in the analytical electron microscope *J. Microsc.* **199** 45–55

[79] Müllejans H and Bruley J 1994 Improvements in detection sensitivity by spatial difference electron energy-loss spectroscopy at interfaces in ceramics *Ultramicroscopy* **53** 351–60

[80] Ballabio G, Bernasconi M, Pietrucci F and Serra S 2004 Ab initio study of yttria-stabilized cubic zirconia surfaces *Phys. Rev. B - Condens. Matter Mater. Phys.*

[81] Malyi O, Klinger L, Srolovitz D J and Rabkin E 2011 Size and shape evolution of faceted bicrystal nanoparticles of gold on sapphire *Acta Mater.* **59** 2872–81

[82] Sternlicht H, Rheinheimer W, Hoffmann M J and Kaplan W D 2015 The mechanism of grain boundary motion in SrTiO3 *J. Mater. Sci.* **51** 467–75

[83] Cheng W C and Wynblatt P 1997 Equilibrium form of Pb-Bi-Ni alloy crystals *J. Cryst. Growth* **173** 513–27

[84] Hondros, E. D., & McLean M 1969 Structure et Propriétés des Surfaces des Solides. (In CNRS conference report) p Vol. 187, 219

[85] Lallet F, Olivi-Tran N and Lewis L J 2009 Interface energies of (100)YSZ and (111)YSZ epitaxial islands on (0001)α-Al2O3 substrates from first principles *Phys. Rev. B - Condens. Matter Mater. Phys.* **79** 1–12

[86] Gibbs J W 1961 *The collected works of J. W. Gibbs*

[87] Baram M, Chatain D and Kaplan W D 2011 Nanometer-thick equilibrium films: The interface between thermodynamics and atomistics *Science (80-.).* **332** 206–9

[88] Kaplan W D 1998 THE INFLUENCE AND CHEMISTRY OF Ca ON INTERFACE IN MELT-INFILTRATED COMPOSITES **46** 2369–79

[89] Gautier M, Fenaud G, Pham Van L, Villette B, Pollak M, Thromat N, Jollet F and Duraud J-P 1994 a-Al2O3 (0001) Surfaces: Atomic and Electronic Structure *J. Am. Ceram. Soc.* **77** 323–34

[90] Alemany P, Boorse R S, Burlitch J M and Hoffmann R 1993 Metal-ceramic adhesion: quantum mechanical modeling of transition metal-alumina interfaces *J. Phys. Chem.* **97** 8464–75

[91] Minesaki Y, Murahara S, Kajihara Y, Takenouchi Y and Tanaka T 2016 Effect of metal conditioner on bonding of porcelain to cobalt-chromium alloy 1–8

[92] Nieva N, Arreguez C, Carrizo R N, Molé C S and Lagarrigue G M 2012 Bonding Strength Evaluation on Metal/Ceramic Interfaces in Dental Materials *Procedia Mater. Sci.* **1** 475–82

[93] Rühle M and Evans A G 1989 Structure and chemistry of metal/ceramic interfaces *Mater. Sci. Eng. A* **107** 187–97

[94] Beck G, Fischer H, Mutoro E, Srot V, Petrikowski K, Tchernychova E, Wuttig M, Rühle M, Luerßen B and Janek J 2007 Epitaxial Pt(111) thin film electrodes on YSZ(111) and YSZ(100) - Preparation and characterisation *Solid State Ionics* **178** 327–37

[95] Amram D and Rabkin E 2013 On the role of Fe in the growth of single crystalline heteroepitaxial Au thin films on sapphire *Acta Mater.*

[96] Kosinova A, Kovalenko O, Klinger L and Rabkin E 2015 Mechanisms of solid-state dewetting of thin Au films in different annealing atmospheres *Acta Mater.* **83** 91–101

[97] Gleiter H 1969 The formation of annealing twins *Acta Metall.* **17** 1421–8

[98] Mahajan S, Pande C S, Imam M A and Rath B B 1997 Formation of annealing twins in f.c.c. crystals *Acta Mater.*

[99] Field D P, Bradford L T, Nowell M M and Lillo T M 2007 The role of annealing twins during recrystallization of Cu *Acta Mater.* **55** 4233–41

[100] Rath B B, Imam M A and Pande C S 2000 Nucleation and Growth of Twin Interfaces in Fcc Metals and Alloys *Mater. Phys. Mech.* **1** 61–6

[101] Carpenter H C H and Tamura S 1924 The formation of twinned metallic crystals *Proc. R. Soc. Lond. A* **106** 463–77

אנרגיה ומורפולוגיה של משטחי ביניים בין

Au ל-ZrO_2

חיבור על מחקר

לשם מילוי חלקי של הדרישות לקבלת התואר מגיסטר למדעים

למדעים בהנדסת חומרים

מאו טינג

הוגש לסנט הטכניון - מכון טכנולוגי לישראל

אלול תשע"ח חיפה אוגוסט 2018

אנרגיה ומורפולוגיה של משטחי ביניים בין **Au** ל-ZrO_2

מאו טינג